APPLICATION OF SURFACE COILS TO IN-VIVO STUDIES USING ^{31}P-NMR SPECTROSCOPY

by

JOYCE SCHACHTER

B.Sc.(Hons.), Simon Fraser University, 1982

A THESIS SUBMITTED IN PARTIAL FULFILLMENT OF

THE REQUIREMENTS FOR THE DEGREE OF

MASTER OF SCIENCE

in

THE FACULTY OF GRADUATE STUDIES

(Department of Chemistry)

We accept this thesis as conforming

to the required standard

THE UNIVERSITY OF BRITISH COLUMBIA

August 1985

In presenting this thesis in partial fulfilment of the requirements for an advanced degree at the University of British Columbia, I agree that the Library shall make it freely available for reference and study. I further agree that permission for extensive copying of this thesis for scholarly purposes may be granted by the head of my department or by his or her representatives. It is understood that copying or publication of this thesis for financial gain shall not be allowed without my written permission.

Department of Chemistry

The University of British Columbia
1956 Main Mall
Vancouver, Canada
V6T 1Y3

Date 19 August 1985

ABSTRACT

The work described in this thesis is divided into two parts: testing and evaluation of some surface coils, and application of the surface coils to *in-vivo* studies. In particular, the localization properties of surface coils were examined and optimized using the highest performance coil geometry and wire. Application of the surface coil technique to *in-vivo* studies involved measuring changes in metabolic status of muscle and brain tissue in rats using ^{31}P spectroscopy.

The properties of surface coils have been studied by evaluating their excitation patterns with ^{1}H and ^{31}P NMR spectroscopy. Surface coils manufactured in different sizes, geometries, and materials were tested for Q factors, signal-to-noise ratios, and pulse widths required for excitation of the sample. A silver plating on the copper wire used to fabricate the surface coils was found to increase the Q and signal-to-noise of the coil. Examination of the excitation patterns of the surface coils with point samples characterized the B_1 field of the coils as decreasing axially and radially from the coil. Calculations of the magnitude of the B_1 field reveal that its dome-like shape extends to approximately one coil radius above the surface coil. It was found that samples lying outside the domain of this

"sensitive volume" did not contribute to a spectrum. These data were all correlated and the "0.9" silver plated coil was deemed to be the most efficient coil with which to pursue further *in-vivo* studies.

In-vivo ^{31}P studies of rat tissues were preceded by *in-vitro* spectral measurements of various metabolites at physiological concentrations. These standards were used to aid in the identification of resonances in the *in-vivo* spectra. Metabolic changes such as artificially induced ischemia in muscle, deceased brain, and artificially induced brain dementia were compared with "normal" ^{31}P spectra of anaesthetized rat tissues. It was found that oxygen deprivation is readily observed with this technique whereas the preparation of brain dementia cannot be diagnosed with ^{31}P NMR spectroscopy.

TABLE OF CONTENTS

LIST OF TABLES

LIST OF FIGURES

Chapter II

Acknowledgement

I would like to thank Laurie Hall for his encouragement and guidance, Edie McGeer and Peter Reiner for their cooperation and support, and Lalith Talagala for many illuminating discussions and his invaluable help. I would also like to acknowledge the assistance of Sarath Abyakoon.

CHAPTER I

INTRODUCTION

The last twenty years has witnessed many changes and advances in the application of NMR to chemical and biochemical systems. From the initial use of narrow bore magnets and liquidus samples, to whole-body tomographs and *in-vivo* imaging, there have emerged many new techniques, new instruments, and a new vocabulary to match. Lauterbur's introduction of NMR imaging[1] and the subsequent furor created a flurry of research activity in this area. Within a few years, the basic tenets of imaging and the scope of experimental techniques were considered sufficiently developed that NMR has again turned its focus. However, along with the impressive technological advances of the 60's and 70's in Fourier transformation and NMR imaging, there has been progress in the science as well.

After the initial introduction of NMR imaging in 1973,[1] many physico-chemical methods were designed to explore the capacities and scope of the technique. Known as the back-projection method, the first imaging experiment differed from conventional NMR simply by the employment of a magnetic field gradient rather than a homogeneous field. In essence, the quantity measured was the density of nuclei (protons) in the sample. Imaging soon became popular while spectroscopy was somewhat overlooked by comparison. The potential applications of imaging in medicine were quickly realized and research was advanced rapidly in this direction. In addition to

new imaging techniques being developed,[2,3] whole-body machines for human *in-vivo* imaging were produced, operating at low fields and using the established back-projection method. The non-invasive nature of this imaging technique contrasted with other methods such as CT, X-rays, PET, etc. used for the possible identification of tumours, multiple sclerosis lesions and other chronic conditions soon made NMR very popular as a medical diagnostic device.

Although *In-vivo* spectroscopy made some progress during the period when NMR imaging was being rapidly exploited, it was left in relative seclusion until the past few years. In addition to proton spectra, other NMR-sensitive nuclei can be used to study the processes of living systems. The most important and promising nucleus is phosphorus which is contained in many of the intermediates involved in bio-energy metabolism, eg. ATP, glucose-6-phosphate, phosphocreatine. Indeed, the first published work of *in-vivo* high-resolution spectroscopy which appeared in 1980, was a ^{31}P spectrum of a rat's leg.[4] The kinetics and thermodynamics of important enzyme-regulated biochemical reactions can be studied with this nucleus as well. Since numerous diseases affect body (including brain) metabolism, the prospect of using the ^{31}P nucleus as a marker for disease continues to be explored. Attempts to achieve clearly resolved proton spectra of biological tissues have, however, met with

difficulties. The most notable of these, the dominance of the water peak, challenged researchers to create new pulse sequences to eliminate or at least reduce this obstruction. There now exists a collection of so-called "water-suppression" techniques[5,6] which are designed solely for this purpose. Other nuclei being used for *in-vivo* spectroscopy include ^{13}C, ^{23}Na, and ^{39}K.[7-13]

Until the last few years, imaging and spectroscopy seemed to be developing along different paths. The two supposedly divergent disciplines started to merge after an interest was expressed in obtaining NMR-type data from a localized region in a sample. Thus, medical users of NMR wished to be able to image specific organs or body parts without interference effects from surrounding tissues; this desire grew out of the intrinsic insensitivity of NMR, the clumsiness of the first imaging devices and the resulting poor resolution of the images. There was also recognized to be a need for high-resolution spectroscopic data from localized regions. Thus the two "hands" of the same body found that they were grappling with the same problem.

Magnet systems with intermediate sized bores, and usually higher fields, were then developed as the basis for equipment used to improve experimental methods. Though much of the early work in "localization" involved studies of perfused organs and excised tissue, this

approach was clearly unsuitable for human patients; hence the quest for new methods of localizing NMR was soon underway. The idea was to obtain as much information as possible from a designated volume of the sample; this would not only include spin density measurements by imaging, but also the very desirable chemical shift data for all pertinent nuclei. Ideally the objective was to be able to choose any arbitrary volume element in the sample from which high resolution spectra would be obtained. This would be a limiting case for localized spectroscopy, and various methods were demonstrably successful in approaching this objective using sophisticated hardware and software combinations.[14,15] Thus, the digression with which NMR imaging had enticed physical chemists returned back to the main science of spectroscopy, but now with a new emphasis: regional localization.

The introduction of surface coils[4] to NMR spectroscopy signified a considerable advance in endeavours to achieve this spatial localization. A surface coil, which is a small loop of wire, serves as the probe used within a conventional super-conducting wide-bore magnet. The simplicity and effectiveness of a surface coil, contrasted with other more sophisticated techniques such as the sensitive point method[15] and Topical Magnetic Resonance (TMR)[16] made the former appear as a very attractive practical tool. Surface coils of various sizes, materials and geometries, activated by a

variety of pulse sequences, have yielded a new and innovative regime of NMR experiments. The key to the localization property of surface coils lies in their excellent filling factor, and their flexibility in both shape and positioning with respect to the experimental region of interest. The current emphasis on *in-vivo* spectroscopy using non-invasive techniques has generated further incentives into research with surface coils. The radio-frequency (rf) magnetic field, or sensitive volume, created by passing current through a surface coil is a hemispherically shaped region which extends to one coil radius from the coil plane at its furthest point. Outside the sensitive volume, the B_1 field is too weak to induce any NMR signals.

There are currently many groups using surface coils for *in-vivo* experiments, since the technique is quite new, operationally simple, and easy to implement. New experimental methods are still being developed even while the theoretical understanding of the coils is broadened and previously unrecognized factors accounted for. Thus, there is now a need to evaluate the current use of surface coils as a means for localizing spectroscopy, and their potentially important role in the future. At the moment there are many users of surface coils but few innovators of surface coil science. One reason for this is that surface coils became very popular, very quickly, precisely because of their simplicity, and widespread use

of the coils by and large preceded a thorough understanding of their properties.

It is essential to fill this gap in NMR spectroscopy and to provide reasonable justification for choosing to use surface coils as the preferred method; this requires that their performance be placed in perspective with other localization techniques. In order to do this, it is imperative to first elucidate fully the properties and limitations of surface coils themselves.

This thesis is an examination of the current status of surface coils in NMR spectroscopy, and the extent of their application to *in-vivo* biological systems. The existing technology regarding surface coils has been evaluated and summarized in Chapter II. Results of this kind have been previously reported in separate accounts, but a general survey and commentary such as this has not previously appeared. In addition, improvements to the design of the coils were made to optimize their performance. Various experimental tests, using chemical phantoms, were performed on the coils to inter-compare their efficiency. In view of the application of the coils to other systems, a coil with appropriate optimal features was chosen for further experimentation.

Chapter III presents a discussion of the application of surface coil technology to *in-vivo* systems. Specifically, the ^{31}P nucleus was used to probe the

metabolic status of brain and muscle tissue in rats. Preliminary *in-vitro* studies consisted of preparing phantoms containing phosphorus metabolites at physiological conditions and obtaining their ^{31}P NMR spectra to be used as standards for peak identification. The *in-vivo* experiments involved application of a physiological insult to the sample prior to spectroscopic measurement. Given that the depth and breadth of knowledge about living systems retrievable via NMR spectroscopy has not yet reached its limits, there remain many unexplored areas, and possible implications and future directions of *in-vivo* ^{31}P experimentation are discussed at the end of the thesis.

CHAPTER II

PROPERTIES OF SURFACE COILS

(2.1) Introduction

The flexibility in design of surface coils has resulted in a sundry collection of various sizes, shapes, and materials. The particular coil used will be determined by the type of experiment being performed as well as the geometry of the sample. In this chapter, choice of the most appropriate coil was based on considerations of the size and shape of a rat's head, as well as the loss of efficiency of the coil in contact with a mildly conducting (i.e. living) specimen.

The most advantageous property of surface coils is their ability to obtain spectra from the region over which they are placed. They localize signals by virtue of their size and rf distribution. What was originally considered a disadvantage of surface coils, namely their inherent production of a nonuniform radio-frequency magnetic field has actually been convenient in the application of rotating frame zeugmatography[17], depth pulses[18-21], and DRESS[22] spectroscopy. Depth pulses, in particular, are well suited to obtaining spectra from regions deeper in the sample which are separated from the surface coil by other layers lying closer to the surface of the specimen. Rotating frame zeugmatography is most useful for compartmentalized organs such as the eye or heart where membranes provide the boundaries defining concentration gradients of metabolites. The particular

sample and experimental objective will determine the degree of localization and hence the method required.

In this chapter, changes in the excitation pattern in the sensitive volume of some surface coils have been examined experimentally. This knowledge helped to determine the experimental parameters and methods required for further *in-vivo* applications. Theoretical studies of the excitation patterns of surface coils have been presented in the literature.[23,24]

(2.2) Theory

Studies employing surface coils have created the need to develop a theoretical understanding of their magnetic and electrical properties as they influence NMR experiments. Various calculations of the induced inhomogeneous magnetic field have presented graphical displays[4,23,24] which aid in understanding the properties of these surface coils, their advantages and limitations.

The magnetic field induced by a current passing through a surface coil can be calculated according to Smythe's equations[25], which are modified versions of the Biot-Savart law. When a unit current flows through the coil wire, the total rf magnetic field produced, B_1, can be divided into an axial component, B_a, and a radial component, B_r, which can rotate through 360 degrees in the xz plane. In this case, the surface coil lies in the

xz plane (see Fig.1(a)). The component of B_1 which rotates over the xy plane, $B_1(xy)$, is of interest since it is orthogonal to the direction of the static magnetic field, B_0, is responsible for changes in magnetization in the sample, and is directly related to receiver coil sensitivity.[26] Surface coils, being both transmitters and receivers are appropriately studied as such.

The radial component, B_r, of B_1 can also be split into two components: $B_r(z)$, parallel to B_0, and $B_r(x)$, perpendicular to both B_0 and B_a (Fig.1(b)). The $B_1(xy)$ vector is composed of an axial component, B_a, and a perpendicular component, $B_r(x)$, directed along the x-axis whose magnitude is determined by the radial vector, B_r. The component of B_r along the x-axis, $B_r(x)$, is given by

$$B_r(x)=B_r\sin\theta \qquad (1)$$

where θ is the angle between B_r and B_0. $B_r(x)$ can now be vectorially added to B_a to obtain the total $B_1(xy)$ produced by the coil (Fig.1(c)):

$$B_1(xy)=B_a + B_r(x) \qquad (2)$$

To calculate $B_1(xy)$, the Smythe equations[25] take the form:

$$B_a = \frac{\mu}{2\pi} \frac{1}{[(b+x)^2 + y^2]^{1/2}} \left[K + \frac{b^2 - x^2 - y^2}{(b-x)^2 + y^2} E \right] \qquad (3a)$$

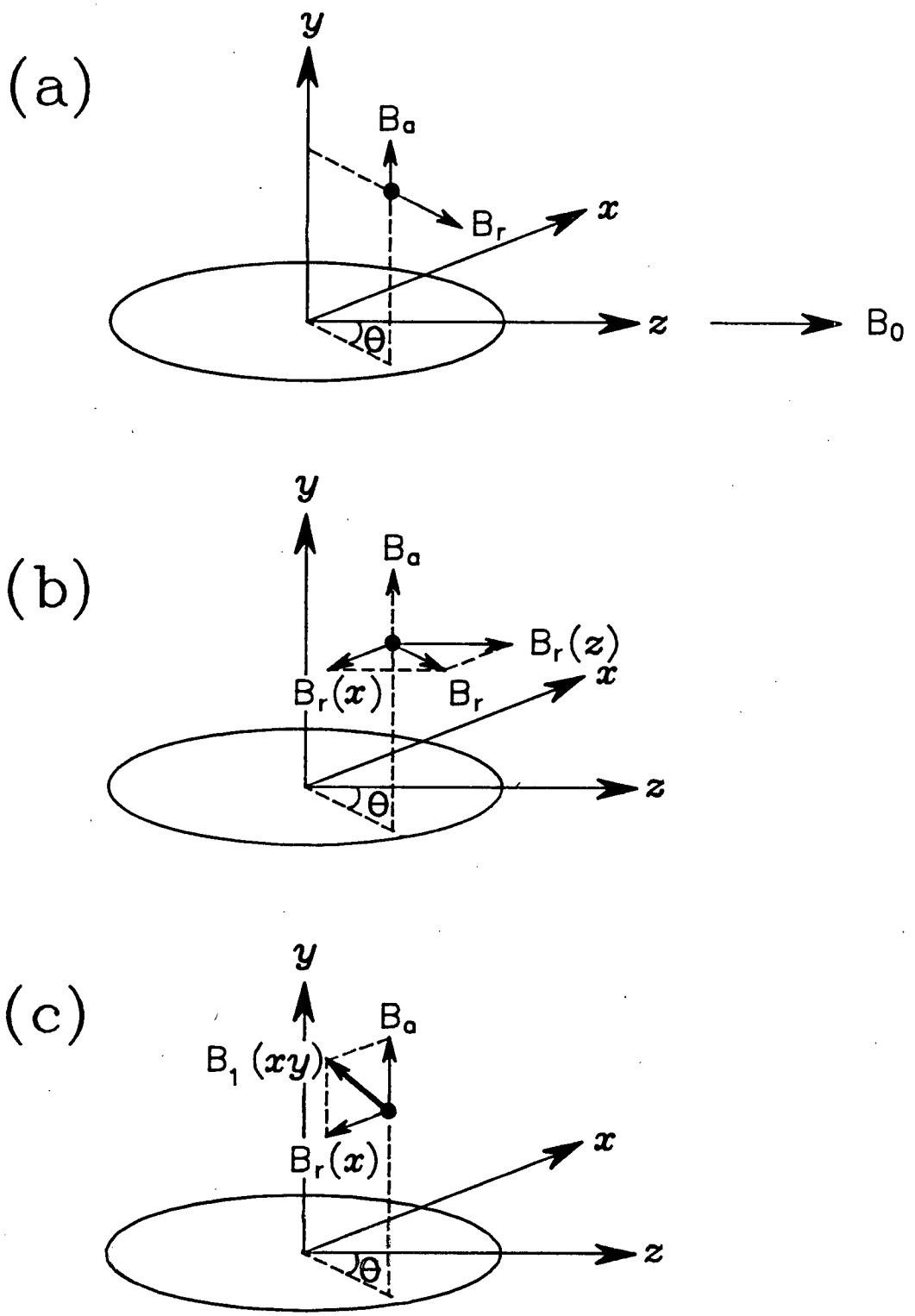

Fig.1 Schematic representation of a single turn surface coil showing rf magnetic field component vectors.

14

$$B_r = \frac{\mu}{2\pi} \frac{y}{x[(b+x)^2 + y^2]^{1/2}} \left[-K + \frac{b^2 + x^2 + y^2}{(b-x)^2 + y^2} E \right] \qquad (3b)$$

where μ is the permeability of the medium about the coil, b is the coil radius, x and y are reduced coordinates (see Fig.1), and K and E are the complete elliptical integrals of the first and second kind.[8-9] A $B_1(xy)$ contour plot is shown in Fig.2 for a single turn coil with a diameter of 2.0 cm. Computer programs used for calculating this and other contour plots can be found in the Appendix. Further contour plots and discussion of coils with different geometry follows later.

The magnetic field induced by a current passing through a surface coil can therefore be seen to diminish in magnitude with increasing distance from the coil plane, and is effectively a radio frequency magnetic field gradient. The region above the coil over which the $B_1(xy)$ field extends, called the "sensitive volume", is dome-shaped in three dimensions, and subtends a hemispherical excitation region with approximately the same radius as the coil (Fig.2(a)).[20] The shape of the sensitive volume depends upon the geometry of the coil. Within the sensitive volume, a series of finite spin planes can be imagined to exist which are coplanar with the surface coil which correspond to the spatial distribution of excitation. These planes of uniform excitation extend radially at least r/2 off-axis and

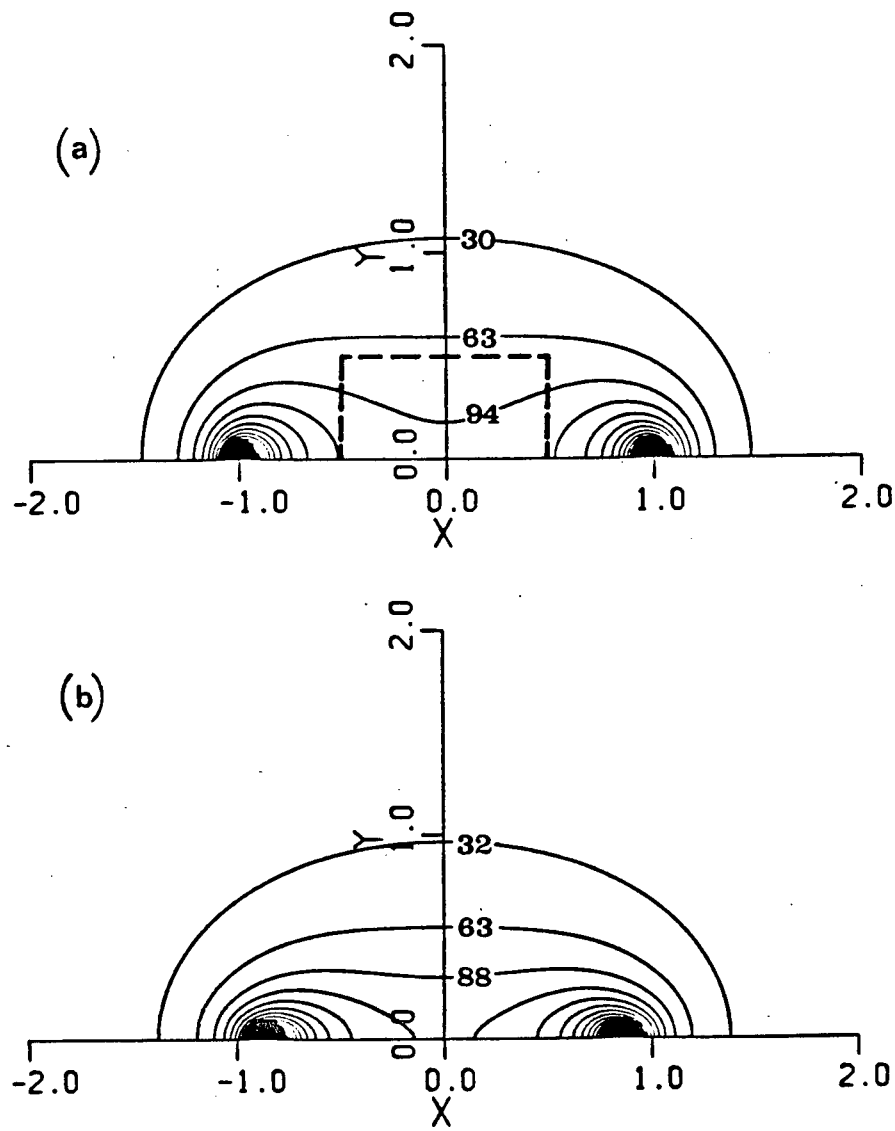

Fig.2 Contour plot of $B_1(xy)$ field of a single turn surface coil with same orientation as per Fig.1; (a) z=0.0; (b) z=0.5 (reduced coordinates). Numbered contours show relative B_1 magnitudes as percentages of B_1 at the coil center.

axially at least r/2 away from the coil plane[20] (dotted line in Fig.2). For any pulse length applied, the nuclei in a sample adjacent to the coil will experience a range of tip angles depending on their respective positions with respect to the coil. Generally, for a pulse width, t_p, applied through the coil, the tip angle, a of nuclei in the sample would be

$$a=\gamma I t_p[B_1(xy)] \qquad (4)$$

where γ is the gyromagnetic ratio of the nucleus of interest, I is the current passing through the coil, and $B_1(xy)$ is the xy component of B_1, the field induced by a unit current passing through the coil. Since $B_1(xy)$ is a spatially dependent quantity, which decreases with increasing axial distance from the coil plane, it cannot be considered as a constant. Therefore, for a predetermined pulse width, the tip angles induced will assume a range of values dependent on the magnitude of $B_1(xy)$ at each particular point. Thus, a is also a spatially dependent quantity. This feature is one of the most important distinctions of surface coils as opposed to conventional NMR probes (solenoid, saddle coils) where a is constant over a large volume of the sample. The diagrams in Fig.3 which are contours of the $B_1(xy)$ of the coils, are also contours of constant tip angle produced by unit current passing through the coils. For example, a pulse producing a 90 degree tip angle at r away from the

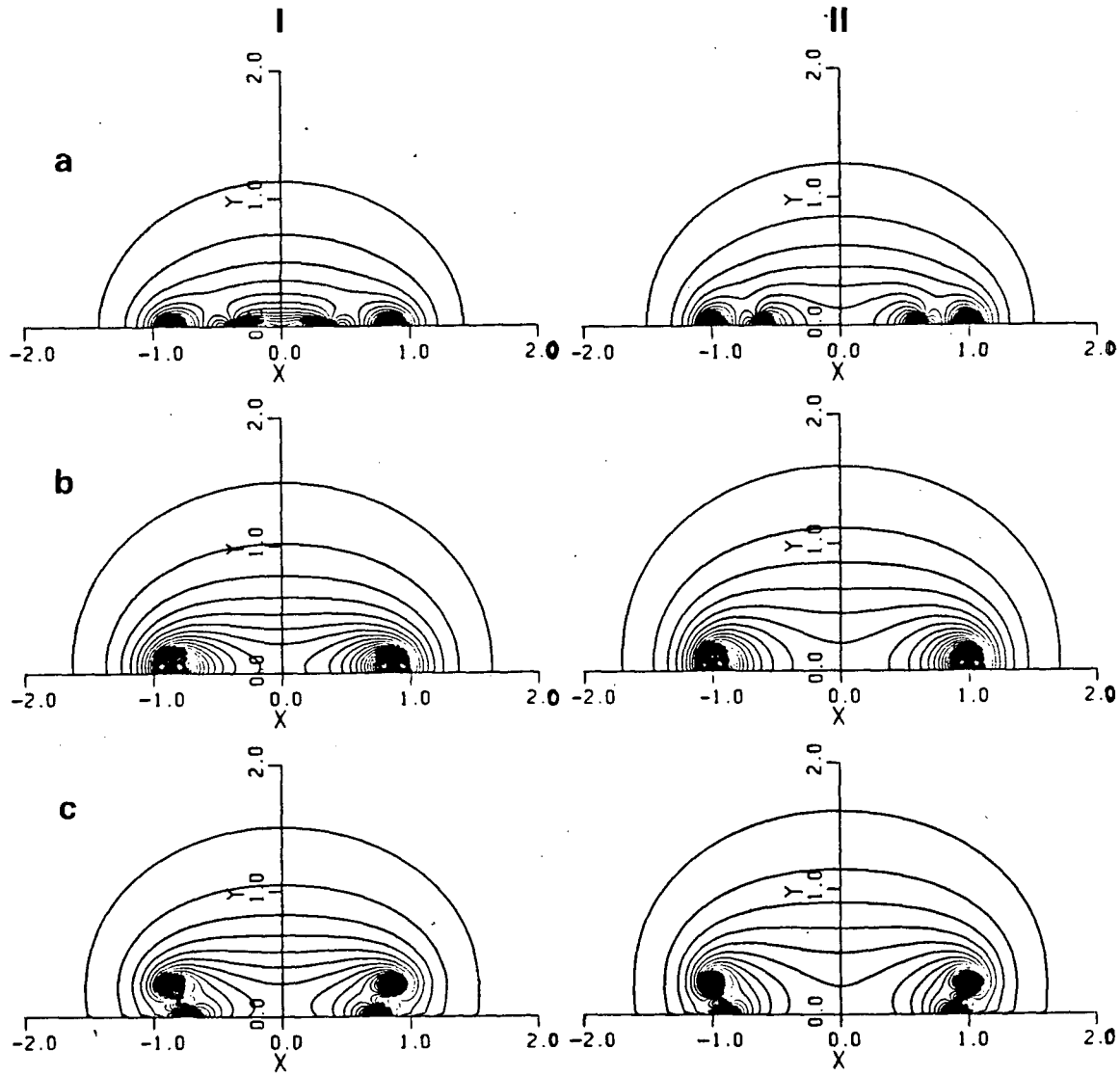

Fig.3 Contour plots for $B_1(xy)$ field of surface coils with same orientation as per Fig.1: (a) flat; (b) double turn; (c) 0.9 coil; column I: z=0.5; column II: z=0.0.

coil center would cause a 30% increase in sensitive volume of the coil compared to a 90 degree tip angle at r/2 for a single turn coil.[24] Generally, longer pulse widths not only increase tip angles close to the coil but also extend the sensitive volume of the coil deeper into the sample. Despite this electronic trick, each of the coils in Fig.4 has a unique pattern of contours which implies the potential depth of its sensitive volume. The general trend of B_1 is to decrease in magnitude as distance from the coil plane increases. Signals coming from regions further than ca. r contribute only marginally to a spectrum and, in fact, experimentally will not appear for samples of uniform shape and homogeneous concentration. This applies to all coils in Fig.4.

Prior to rf excitation, the equilibrium magnetization of the sample, M_0, is aligned with the main magnetic field, B_0. This magnetization interacts with applied radio-frequency waves by rotating away from B_0 to some angle α (Eqn.4). The component of magnetization in the xy plane, M_{xy}, is the source of the NMR signal received:

$$M_{xy} = M_0 \sin\alpha \qquad (5)$$

Sample regions lying closer to the coil plane experience a stronger $B_1(xy)$ field than regions further away.

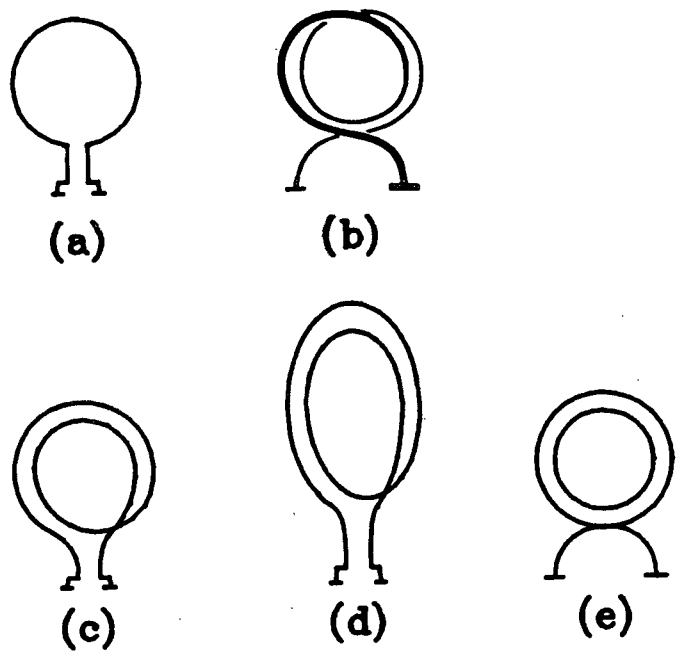

Fig.4 Schematic representation of surface coils tested: (a) single turn; (b) double turn; (c) flat; (d) elliptical; (e) 0.9 coil.

Similarly, magnetization M_{xy} lying close to the coil plane induces a stronger signal in the coil than M_{xy}, of the same magnitude, situated further away. This behavior, known as the principle of reciprocity,[27] is an expression of the dual dependence of the NMR signal, S, on $B_1(xy)$ in experiments where a single coil is used for transmission and reception[23] (see Eqn.4 and 5).

$$S \propto B_1(xy)\ M_{xy} \qquad (6)$$

The signal-to-noise value is affected not only by the magnitude of the signal itself, but also by the effects of different types of noise. Noise is a composite quantity which arises from two sources: resistivity of the coil itself, and noise generated by the sample. The latter of these is a combination of magnetic and dielectric losses which are important to consider for "lossy" or conductive samples. Signal-to-noise also depends on the fraction of the sensitive volume which is occupied, called the filling factor. Surface coils, being flexible in size and shape have characteristically excellent filling factors. A high quality factor, Q, will improve a coil's signal-to-noise as will other factors pertaining to the electrical properties of the coil as well as the entire circuit. For a detailed discussion of signal-to-noise ratios, the reader should read reference 28.

(2.3) Surface Coils and Q Factor

The quality factor, Q, of a receiver coil, such as a surface coil, is a function of the coil's inductance, L, and resistance, R:

$$Q = L\omega/R \tag{7}$$

where ω is the resonant frequency of the circuit. The Q of the resonant circuit can be regarded as a magnification factor that determines how much the voltage across L or the capacitance, C, is increased by the resonant rise of current in a series circuit.[29] The Q factor is important since both B_1 and signal-to-noise are proportional to its square root. A high Q factor will increase both these quantities which are desirably optimized at higher values. During the tuning process, the capacitance of the receiver coil circuit is adjusted so that

$$LC\omega^2 = 1 \tag{8}$$

which is the resonance condition for a series circuit. The inductance of the coil, which is slightly sensitive to the type of sample present, therefore influences the sharpness of the circuit's tuning. Eddy currents produced in "lossy" or conductive samples by the B_1 field cause a decrease in the coil's inductance and hence a lowering of the Q factor.

The Q factors of various coils were measured and are listed in Table I. Values for loaded and unloaded coils are shown. The coils were loaded by resting a human arm on them. In this way, the efficiency of the coil, while performing in an actual experiment was clarified. An average loss of 40% efficiency was noted upon loading the coils connected with a double-tuned circuit (^{31}P and ^{1}H). Single-tuned circuits suffer an even larger reduction in efficiency when they are loaded; these probes have higher initial values and consequently show higher overall efficiency. Most of the studies of phantoms were performed with a double-tuned circuit probe, but the rat spectra were taken with a single-tuned probe.

Initially, the surface coils manufactured for these experiments were constructed from hollow copper tubing. This produced surface coils of reasonable efficiency: a 4.5 cm diameter single turn coil with a Q of 150 is typical for this size, shape and material. Smaller coils were more desirable for the planned *in-vivo* spectra; the geometries shown in Fig. 4 were adopted by necessity or suggestions from the literature.[2,30,31] Generally, the coils with two turns, whether flat, or adjacent, produce larger sensitive volumes than single turn coils, as shown in Figs.2 and 3. In addition, both double turn coils, in which the two loops are not coplanar, produce larger sensitive volumes than the double turn flat coil. This subtlety influences the efficiency of the coils and the

Table I Q Factors for some surface coils

(^{31}P) (^{1}H)

		2 cm 0.9 Ag/Cu	4.5 cm single turn Cu	2 cm flat Ag/Cu	2 cm single turn Ag/Cu
double tuned circuit	unloaded		154 **245**	155 **250**	
	loaded		140 **52**	88 **164**	
single tuned circuit	unloaded	200	360	250	100
	loaded	95	155	180	100

diversity of their applications to various experiments.

Thin copper wire was used for construction of smaller coils, until it was found that a silver coating on the copper wire increased coil efficiency. This follows from the better conducting properties of silver and the well-known flow of current along the surface of a wire. Perusal of Table I reveals that the flat coil has the highest loaded Q factor and the 0.9 coil the lowest. However, further considerations of the signal-to-noise ratio, which will be discussed later, provided strong arguments to show that this coil was not the most appropriate for future *in-vivo* experiments.

(2.4) Signal-to-Noise and the 90 Degree Pulse

A good indication of the efficiency of a surface coil and its potential for yielding good signal-to-noise is the width of the 90 degree pulse at the coil center. A number of experiments were performed to determine the proper pulse width for some of the coils in Fig.4. First, a small beaker, with the diameter of the surface coil, was filled with water and placed on the coil. A number of one pulse experiments were performed with the pulse width varied systematically in regular increments. The resulting data in Fig.5 shows asymmetric curves which increase to a maximum and then decrease with a slope unique to each coil. In view of the rf magnetic field gradient created by the surface coil, the graphs must be

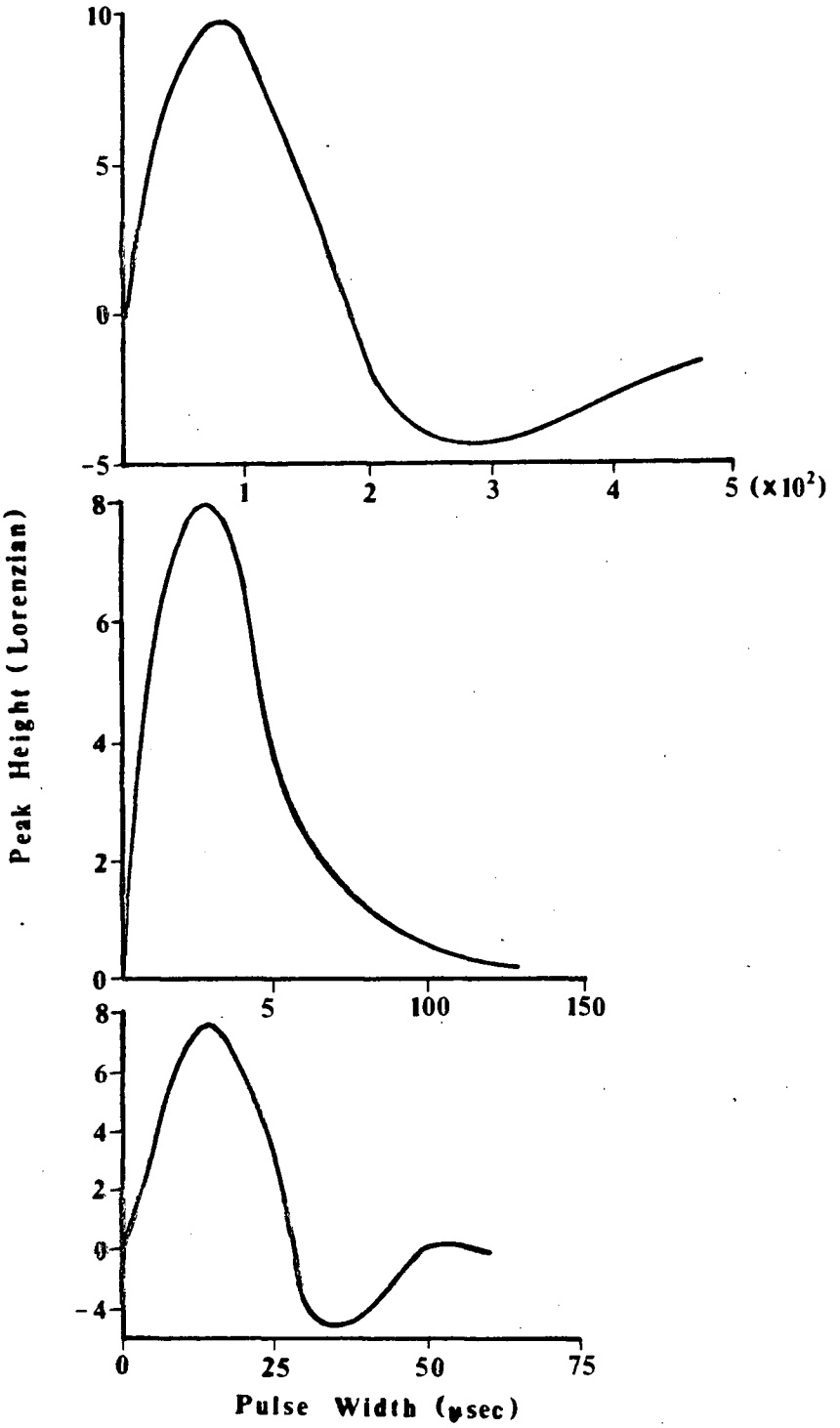

Fig.5 Peak height vs pulse width for 90 degree angle determination; top: 4.5 cm single turn Cu coil; middle: 2 cm double turn Ag/Cu coil; bottom: 2 cm flat Ag/Cu coil.

interpreted carefully since the sample is not experiencing a uniform B_1 field. Even though the sample has a uniform spin density, i.e. a beaker of water, signal intensity changes in moving from the plane of the coil to regions axially further away due to the change in the rf field. Since the curve represents the signal accumulated for the sample occupying the entire sensitive volume of the coil, the maxima in these graphs must correspond to the pulse width which induces the largest spatially averaged tip angle in the sample. Once pulse widths become longer than this optimum value, contribution from signals with tip angles greater than 180 degrees arising from some regions within the sensitive volume, are increased and will be subtracted from the total signal, causing a decrease in total peak height. In addition, the region of the sample experiencing a 90 degree pulse is further away from the coil where the B_1 field is weaker. In consideration of the principle of reciprocity, this nuclear induction signal will be weaker as well. The shape of the curve for the flat coil (Fig.5(c)) differs from the rest. The second rise of the curve results from the interaction of the fields of the small and large loops which creates a region close to the coil that yields a small positive signal when most of the sample's nuclei are subjected to a ca. 180 degree pulse.

Using the pulse width measured from the maxima of the curves in Fig.5, the first series of tests for signal-to-noise were done. Fig.6 shows the results of these tests. Here, the effects of coil geometry and material are most apparent. The two double turn coils had the same geometry and dimensions, only differing by the fact that one was silver plated. A comparison of coil geometry was made between two silver plated copper coils each of diameter 2.0 cm (Fig.4b-4c). In each of these cases, an increase of 35-40% in signal-to-noise was noted with the coil which yielded the higher signal-to-noise ratio. The silver plating increased signal-to-noise by 40% and the geometry factor caused an improvement of 35%. These changes are significant and should be considered when designing coils. It should be noted that the experiments used to test signal-to-noise will also be a reflection of the extent of the sensitive volume of the coils, except in cases where coil geometry was constant and only coil material varied. In consideration of this fact, measuring signal-to-noise per unit volume rather than the entire sensitive volume would provide more illuminating data. Estimates of sensitive volumes were made by approximating the radius of the lowest valued contour in Figs.2 and 3 and calculating the volume of a hemisphere. This revealed that the signal-to-noise values reported in Fig.6 magnify the differences between the tested coils but show the same trend as signal-to-noise

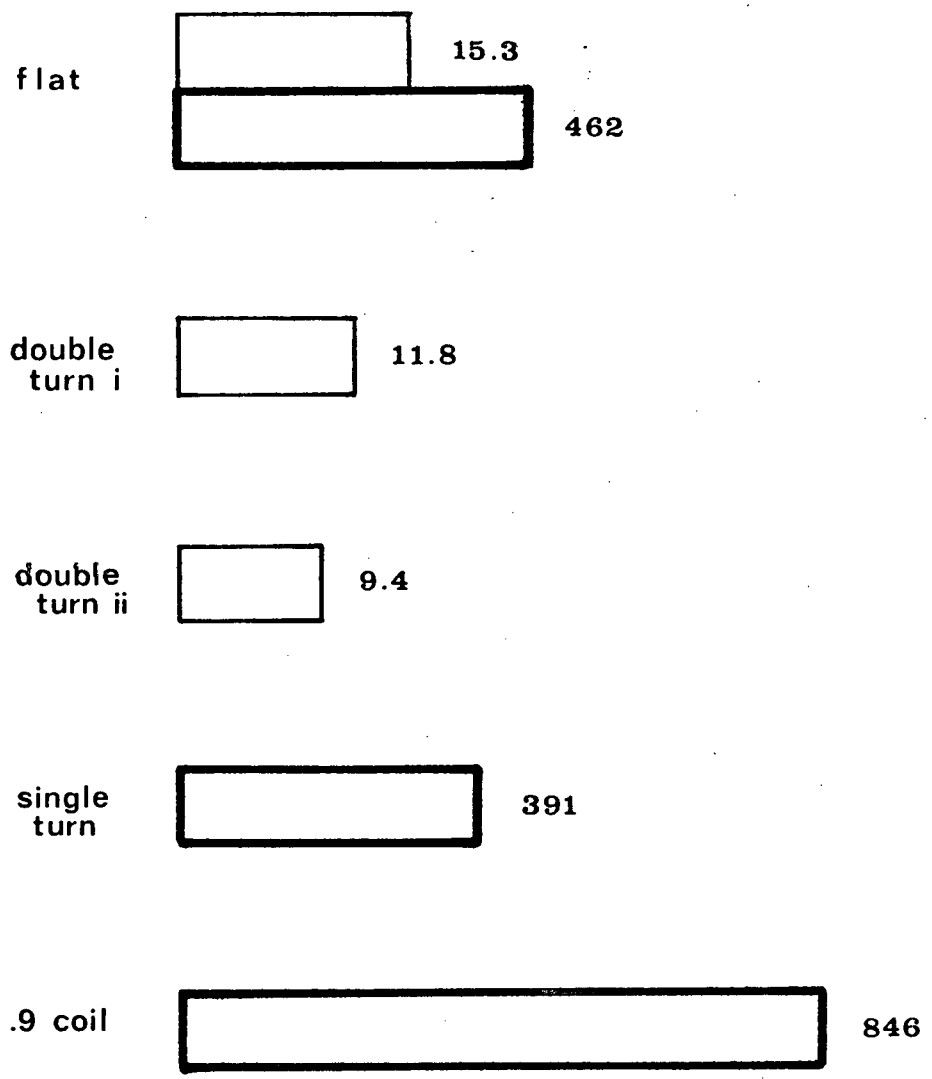

Fig.6 Signal-to-noise ratios for various coils; thin line: 5 ml beaker of 100 mM Na_2HPO_4; thick line: 100 ml beaker of H_3PO_4 (85%); (i) Ag/Cu coil; (ii) Cu coil.

per unit volume values. The only exception to this was the 2 cm single turn coil which showed a lower signal-to-noise than the flat coil but higher signal-to-noise per unit volume. Signal-to-noise values were all enhanced with the use of copper rf shields fitted across the ends of the magnet bore. This is a good practice in any case where the magnet and spectrometer are not well isolated from external rf interferences.

A recent advance[32] in surface coil design incorporates a Faraday shield as a matrix for the coil wire; the entire ensemble resembling a thick coin. This type of shielding is apparently more effective than a teflon coating for the wire and the coil is still lightweight and portable; thus the shielding detracts little from the coil's mobility over the sample.

Another example of the influence of geometry and material was clearly shown with the 0.9 type coil. The diameter of this coil was ca. 2.0 cm with the exact geometry outlined in reference (31). In addition, a slightly thicker wire was used which was also plated with silver. The 0.9 coil registered much higher signal-to-noise than any of the other coils. The geometry of this coil characterizes a B_1 magnetic field which extends axially further into the sample than any of the other coils (see Fig.3(c)). The linearly decreasing magnetic field gradient of this coil is a feature which

simplifies the excitation pattern within the sensitive volume and would ensure a more uniform signal induction than would a nonlinear B_1 field. The depth into the sample of the region of interest will determine the type of coil used. For experiments which require shallow surface spectra, the flat coil would be more appropriate. The 0.9 coil is more useful for obtaining information from a sensitive volume up to a depth of at least one radius, and presently works best with specimens of uniform composition although efforts are underway to achieve further localisation within the sensitive volume.

(2.5) Two and Three Point Experiments

The two and three "point" experiments were developed to test the effect of the B_1 gradient on the sample region of interest. The "points" were made from the bottoms of 5 mm NMR tubes, filled with water so that they approximated a sphere, or drop, of water. In the three "point" experiment, the 4.5 cm single turn Cu coil was used and the "points" were placed along the coil axis at 0, r/2, and r away from the coil center. These "points" of water were used to approximate small volume elements within the sensitive volume of the coil over which $B_1(xy)$ could be considered to be constant. By eliminating the variability of $B_1(xy)$ over the sample volume, it would be possible to observe differences in tip angle, and frequency of signal amplitude modulation with pulse width

within the sensitive volume. Two and three "point" experiments were done to compare these effects with two surface coils of differing size, geometry and material. A static magnetic field gradient was applied coaxially to the coil to induce a resonance frequency shift between the "point" phantoms. Gradients in the B_1 field will not interfere with the resolution of details of chemical shift, unlike B_0 gradients, which act similarly to electronic shielding.[33] The B_0 field was shimmed to observe a single water peak to ensure that both "points" experienced the same magnitude of the linear applied gradient.

The pulse sequence and resulting spectra are shown in Fig.7. The pulse width was systematically increased from 10 to 75 μsec in increments of 5 μsec with a delay of 10 sec between experiments. Initially the signal intensity from all "points" increases with the pulse width but because the "point" in the coil plane is subject to higher $B_1(xy)$ field than the "points" at r/2, and r, its magnetization experiences a greater tip angle for a given pulse width, e.g. 180 degrees, while the "point" at r/2 is tipped only slightly more than 90 degrees. Fig.8 is a manifestation of the difference in amplitude modulation of the "points" as a function of their respective positions with respect to the coil plane. Since the tip angle (Eqn.4) induced at the two "points" is different, the signal, S, received from the

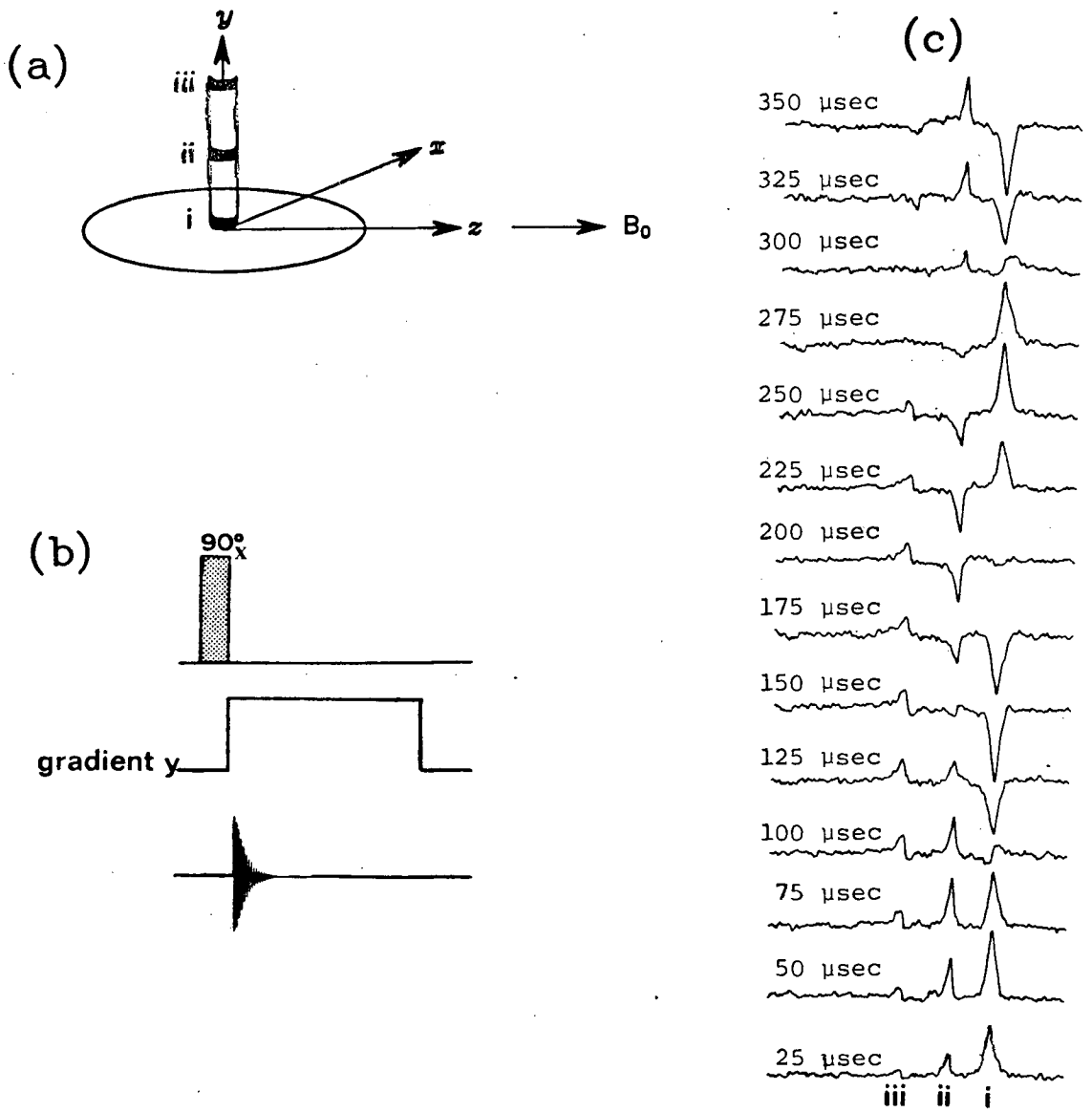

Fig.7 (a) Schematic representation of configuration of three "point" sources above surface coil; (b) pulse sequence employed in two and three "point" experiments; (c) spectra for three "point" sources of H_2O. Roman numerals correspond to sample "points". (spectral width=±1000 Hz; scans=1; block size=1024 points; pulse width=25-500 μsec (δ=25 μsec); relaxn delay=0.5 sec; y gradient=0.04 G/cm; line broadening=10 Hz)

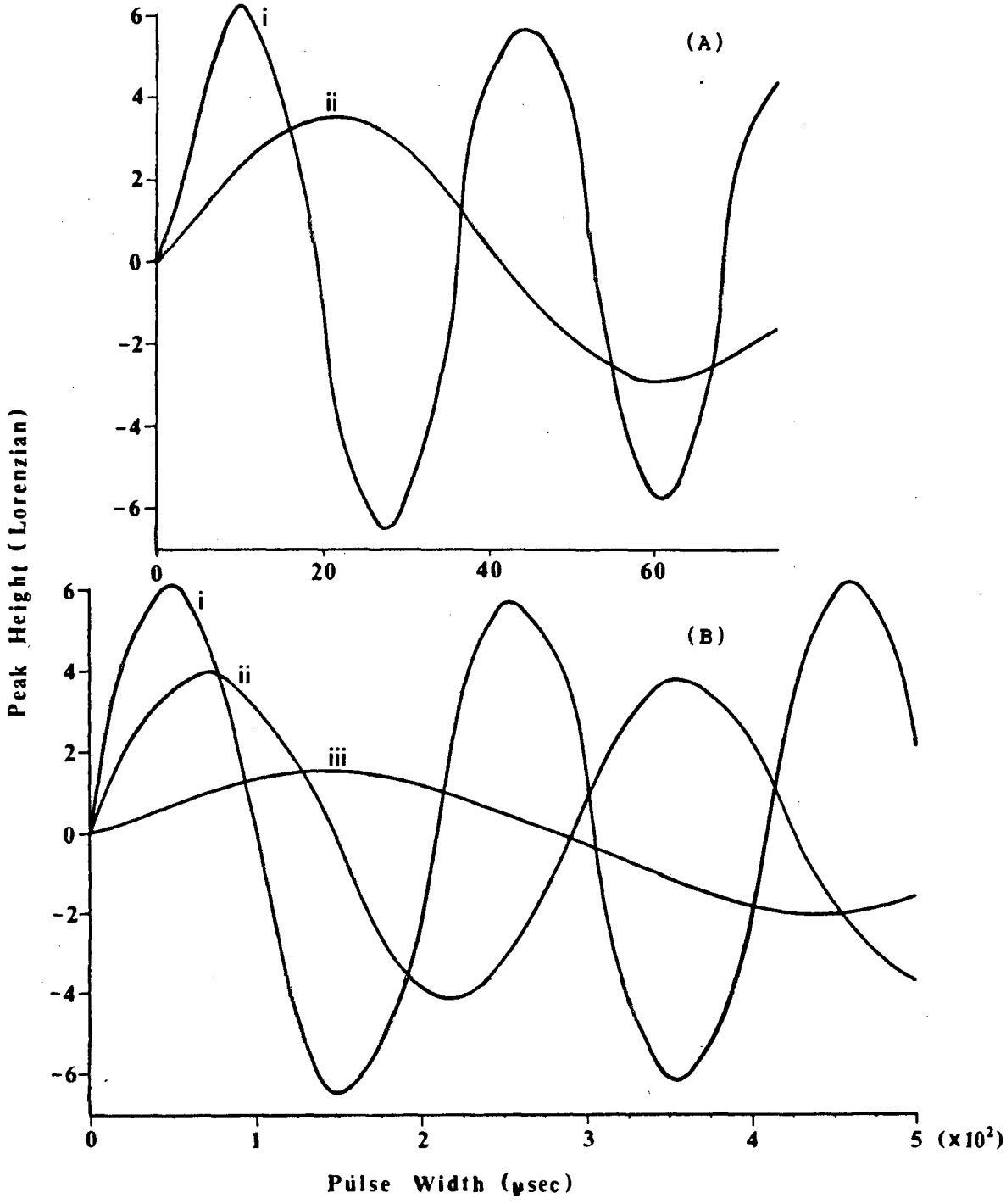

Fig.8 (A) Peak height vs pulse width for two "point" sources of H_2O using 2 cm flat Ag/Cu surface coil; (B) peak height vs pulse width for three "point" sources of H_2O using 4.5 single turn surface coil. Roman numerals correspond to sample "points" shown in Fig.7(a).

two "points" will also be different:

$$S = M_0 \sin a \tag{9}$$

where substituting for a yields

$$S = M_0 \sin\{\gamma I t_p [B_1(xy)]\} \tag{10}$$

The frequency of amplitude modulation with pulse width, (t_p) for each "point" is then

$$f = \frac{\gamma I [B_1(xy)]}{2\pi} \tag{11}$$

which will be unequal for the two "points" because $B_1(xy)$ at the "points" is different. The rate of amplitude modulation of the signal decreases with increasing axial distance from the coil.

Another "point" experiment was done using two "points" placed along the coil axis at 0 and r/2 away from the coil center using the 4.5 cm single turn copper coil. Fig.8 shows the effect of the B_1 gradient on peak height and amplitude modulation for the two and three "point" experiments. Despite the use of two different surface coils, the pattern of amplitude modulation of the "points" is similar. It is expected that the "point" located in the coil plane would produce the highest resonance peak heights and have the highest frequency of amplitude modulation since $B_1(xy)$ is at a maximum there

(Eqns.8 and 9). The "point" at r away from the coil plane would produce a signal with lower peak height and amplitude modulation frequency since it is situated in a region of relatively weaker $B_1(xy)$ field. Fig.8 shows these effects clearly for the two and three "point" experiments. A selected, though broad, region of sample volume can potentially be isolated depending on the pulse width used. The most notable difference between the graphs for the two coils is in the pulse width required to produce a 90 degree tip angle in each "point". However, this has no bearing on the objective of this experiment.

Selective sampling by choosing appropriate pulse widths works reasonably well for discrete phantoms; for example, at a pulse width of ca. 100 μsec, the "point" in the coil plane undergoes a 180 degree flip but the magnetization at r/2 is at ca. 100 degrees, hence a high-resolution spectrum could be obtained with minimal contributions from the former "point". However, in a continuous specimen, some interference could arise from regions which have magnetization flipped to angles intermediate between 90 and 180 degrees; localization of signals within the sensitive volume of a surface coil by varying the pulse width can be achieved with phantoms but is not reliable for precise *in-vivo* applications.

(2.6) Capillary Tube Experiments

The two and three "point" experiments gave evidence for the potential to separate signals based on their spatial coordinates. The next step was to determine how thin and wide the isolated region could be. This would show more clearly how the rate of amplitude modulation decreased characteristically for each surface coil. Twenty-four capillary tubes (I.D. 1.5 mm, O.D. 3.0 mm, length 5 cm) were arranged into six rows of four tubes each. Each row defined a plane of water 1.5 mm thick separated from the adjacent plane by a distance of 1.5 mm. Fig.9 shows the ideal and experimental dimensions of the phantom. This phantom was used with both water (^{1}H) and phosphorus acid (^{31}P). The pulse sequence depicted in Fig.7 was used with a static magnetic field gradient which was three times the magnitude of that used in the "point" experiments. This was required to clearly separate the resonance frequency shifts of the sample planes. Pulse widths were varied as before and the resulting spectra are shown in Fig.10. Clearly, the use of short pulse widths allows only the region closest to the coil to contribute to a spectrum; that is, the sensitive volume of the coil extending to ca. r from the coil plane (Fig.2). Sample lying near the coil wire experiences a greater amplitude modulation than that further away, and there is a "point" when the region closest to the coil, i.e. 2.5 mm from the coil plane,

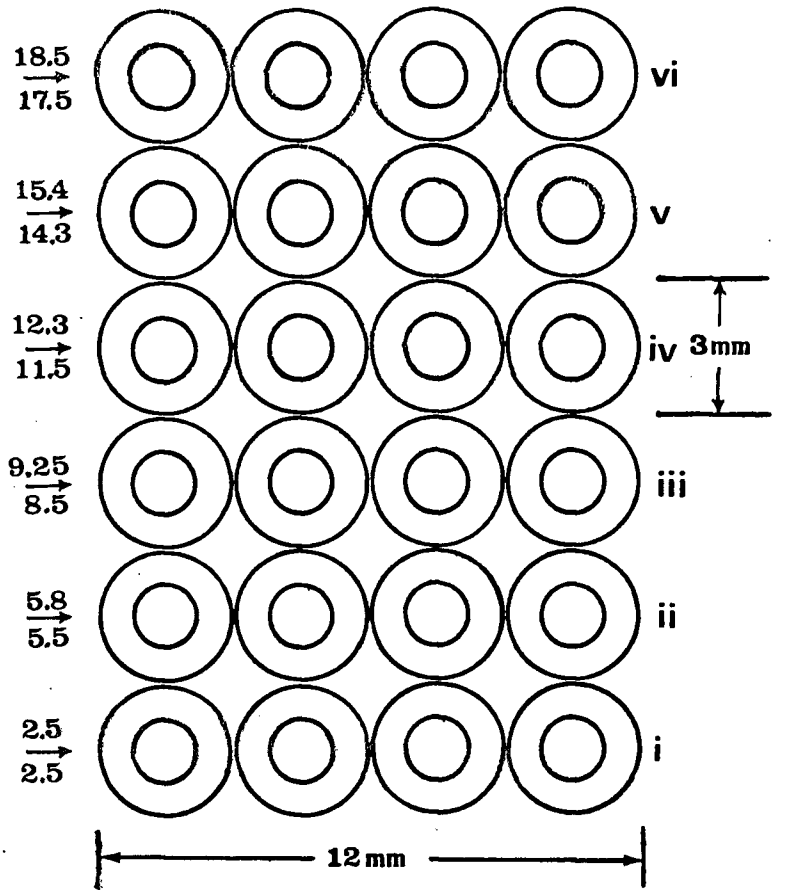

Fig.9 Schematic cross-section of capillary tube phantom. Numbers below arrows are ideal dimensions (mm); numbers above arrows are actual averaged dimensions of the height of each row of tubes from the base. Roman numerals correspond to phantom planes.

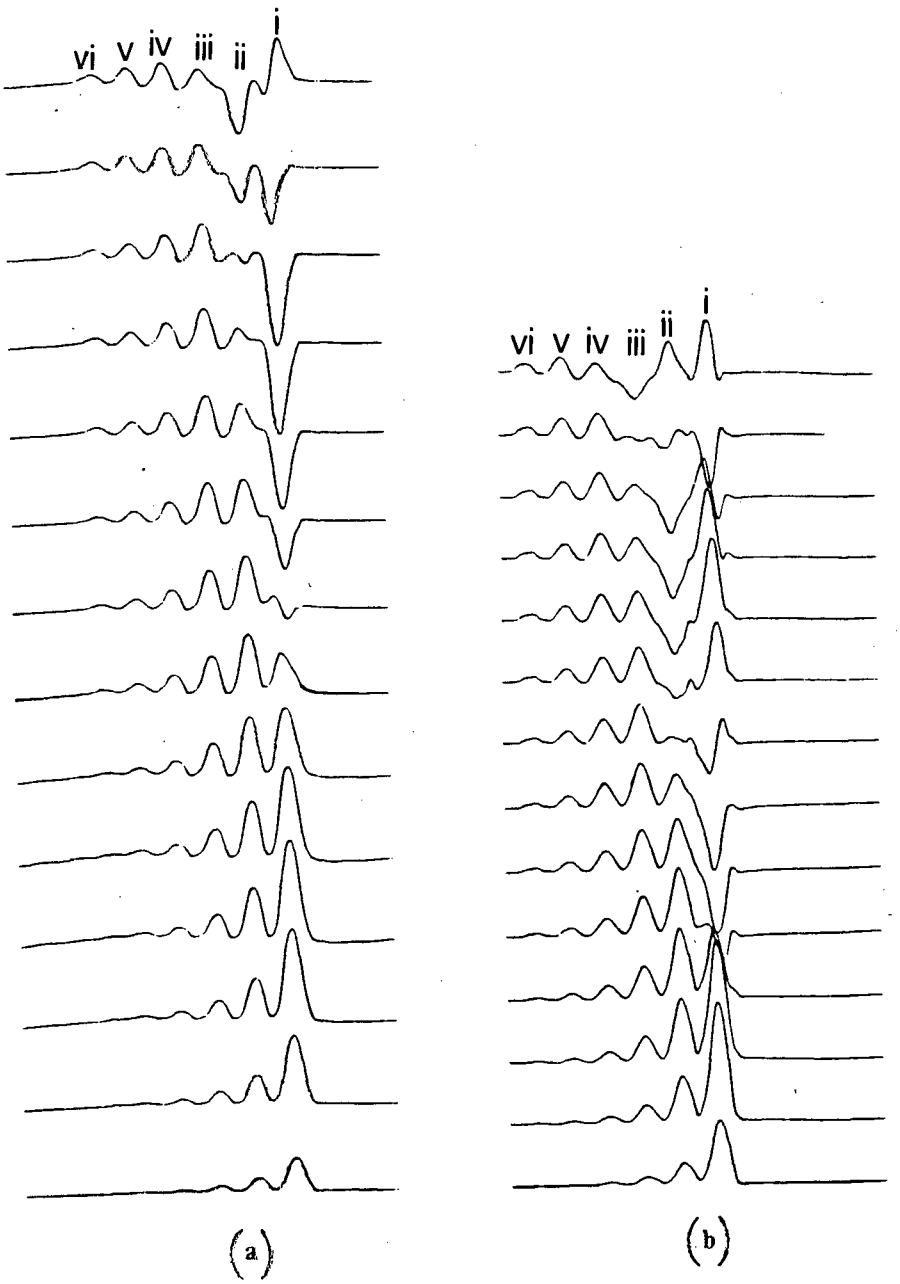

Fig.10 Spectra from H_2O capillary tube phantom excited with pulse widths from 5 - 70 μsec in 5 μsec increments; (a) 2 cm flat Ag/Cu coil; (b) 2 cm double turn Ag/Cu coil. Roman numerals correspond to phantom planes in Fig.9. (spectral width=±1000 Hz; scans=1; block size=2048 points; pulse delay=0.5 sec; y gradient=0.13 G/cm; line broadening=10 Hz)

will undergo a 180 degree flip while the spins 5.5 mm from the coil plane are being tipped by some angle which leaves a resultant magnetization in the xy plane. In particular, the signal from nuclei close to the coil can be minimized (180 degrees) when signals further away from the coil are maximized (90 degrees). This can be seen for both flat, and double looped configurations where the dispersion-like signal indicates a flip angle of 180 degrees. It should also be noted that at ca. 40 μsec for the flat coil, both planes nearest the coil, i.e. the entire area up to r/2 away will not contribute to the spectrum thus allowing spectral viewing of the region between 8 and 11 mm into the sample.

Peak amplitude modulation vs pulse width plots are shown in Fig.11 for a variety of coils. Features of note in these graphs are the "points" where signal intensity of one plane vanishes while another plane is maximized. This occurs at 23 μsec and 40 μsec in Fig.10(b) where the signals from the first plane and then from the entire region up to ca. r are minimized. The double turn silver plated coil has a different pattern of rising signal intensities and indeed these patterns are unique and characteristic to each coil. Longer pulse widths must be applied to achieve the same flip angle due to this coil's lower Q. In this case, the only volume which could potentially be isolated with a specific pulse width is the region between r/2 and r, however, this is a fairly

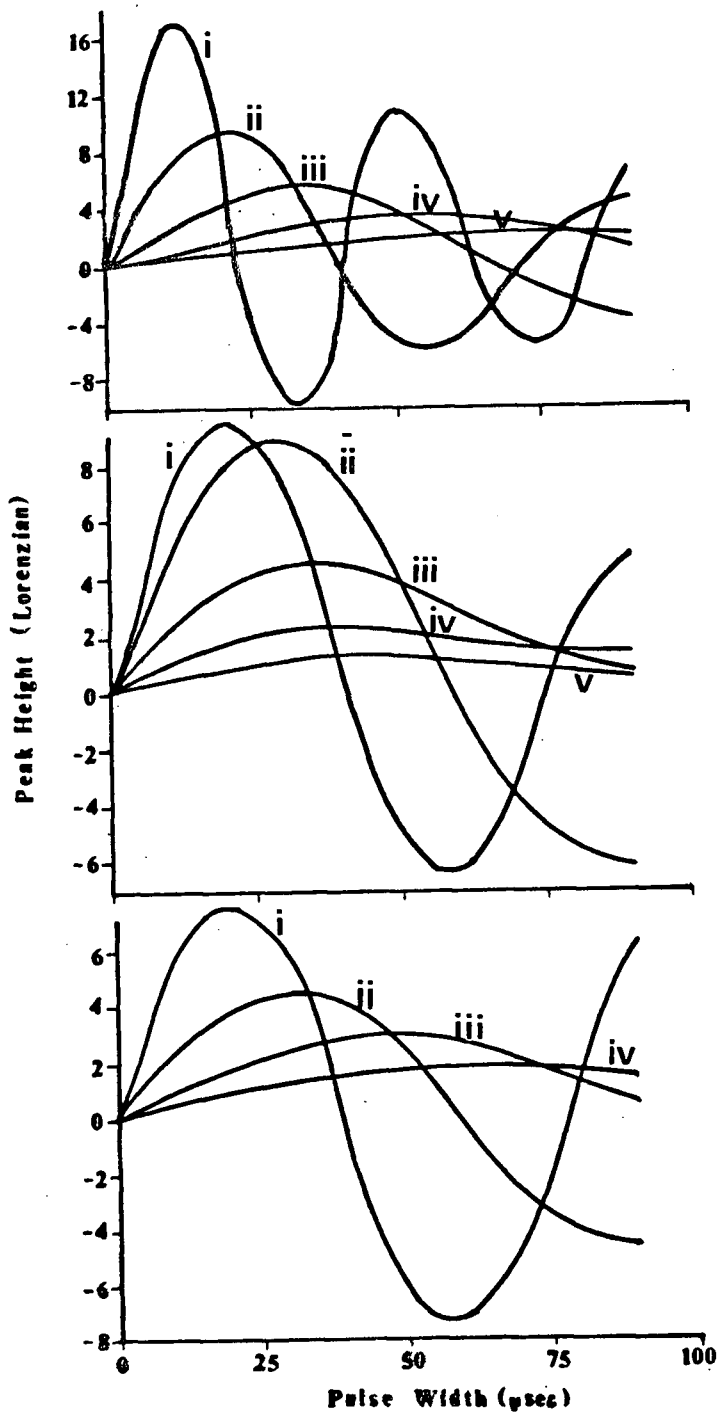

Fig.11 Peak height vs pulse width for rows of H_2O in capillary tube phantom; top: 2 cm flat Ag/Cu coil; middle: 2 cm double turn Ag/Cu coil; bottom: 2 cm double turn Cu coil. Roman numerals correspond to phantom planes in Fig.9.

thick slice: 5 mm for a surface coil of 2 cm diameter.

These same experiments were repeated with phosphorus acid, H_3PO_2, to test the response of ^{31}P nuclei (see Fig.12). The only difference in these graphs should be an increase in pulse width by a factor of the ratio of the nuclear gyromagnetic ratios of ^{31}P to ^{1}H. In practice, the general pattern of signal intensity and amplitude modulation for all the planes was found to be the same, whether ^{1}H or ^{31}P was measured.

The elliptical coil was tested for its 90 degree pulse length, (^{1}H and ^{31}P) and for its ability to separate signals using the capillary tube phantom (^{31}P only, Fig.13). The pulse widths producing the largest peak height differ by a factor of ca. 1.5 which is 60% of the gyromagnetic ratios. The shape of the curves for the elliptical coil bears similarities to both coaxial and flat silver plated coils. It is similar to the coaxial coil in that at both r/6 and r/2, the sample is excited with pulse widths of similar values whereas with the flat coil, these two regions require very different pulse widths to achieve a 90 degree tip angle. The similarity to the flat coil exists in the pattern of amplitude modulation of the first two planes of the phantom. When the first plane undergoes a 180 degree spin flip, the spins in the second plane are at ca. 90 degrees, whereas for the coaxial coil, the magnetization is closer to 120

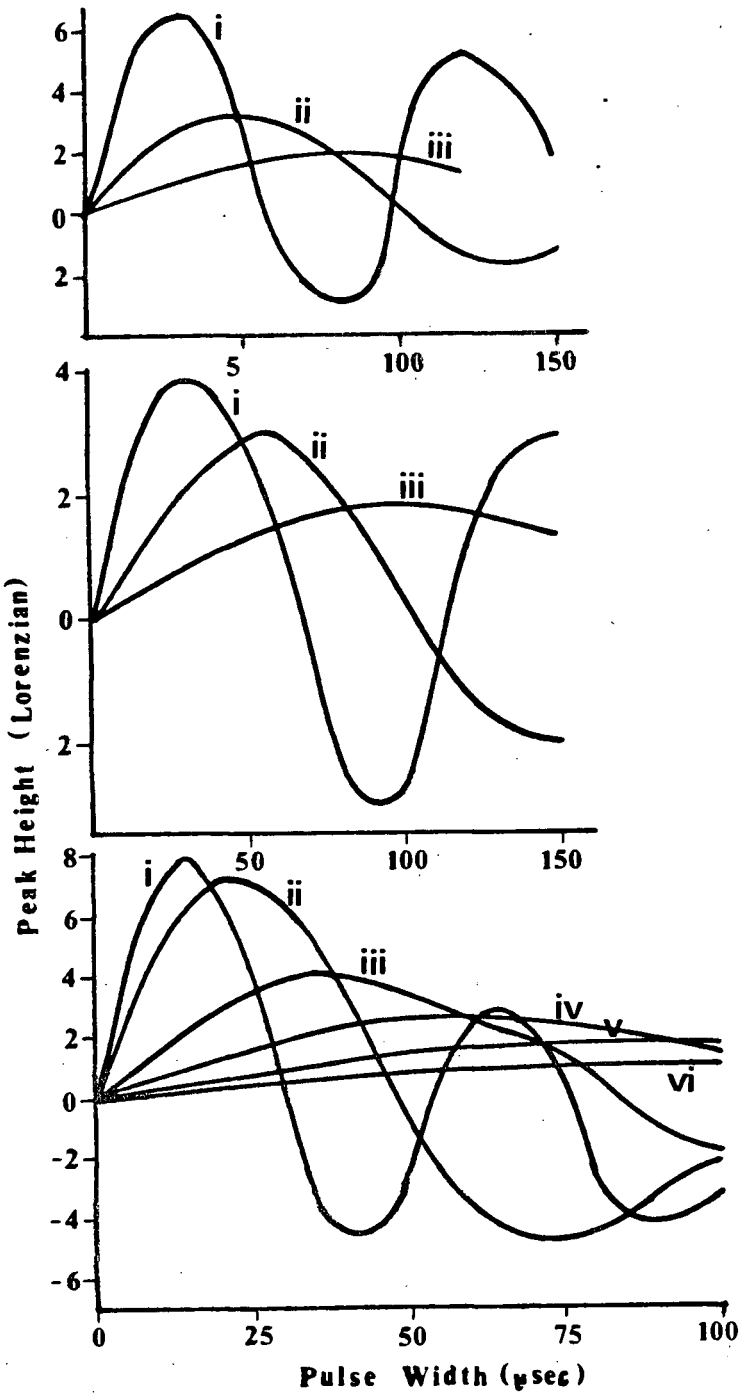

Fig.12 Peak height vs pulse width for rows of H_3PO_2 in capillary tube phantom; top: 2 cm flat Ag/Cu coil; middle: 2 cm double turn Ag/Cu coil; bottom: oblate eliptical Ag/Cu coil. Roman numerals correspond to phantom planes in Fig.9.

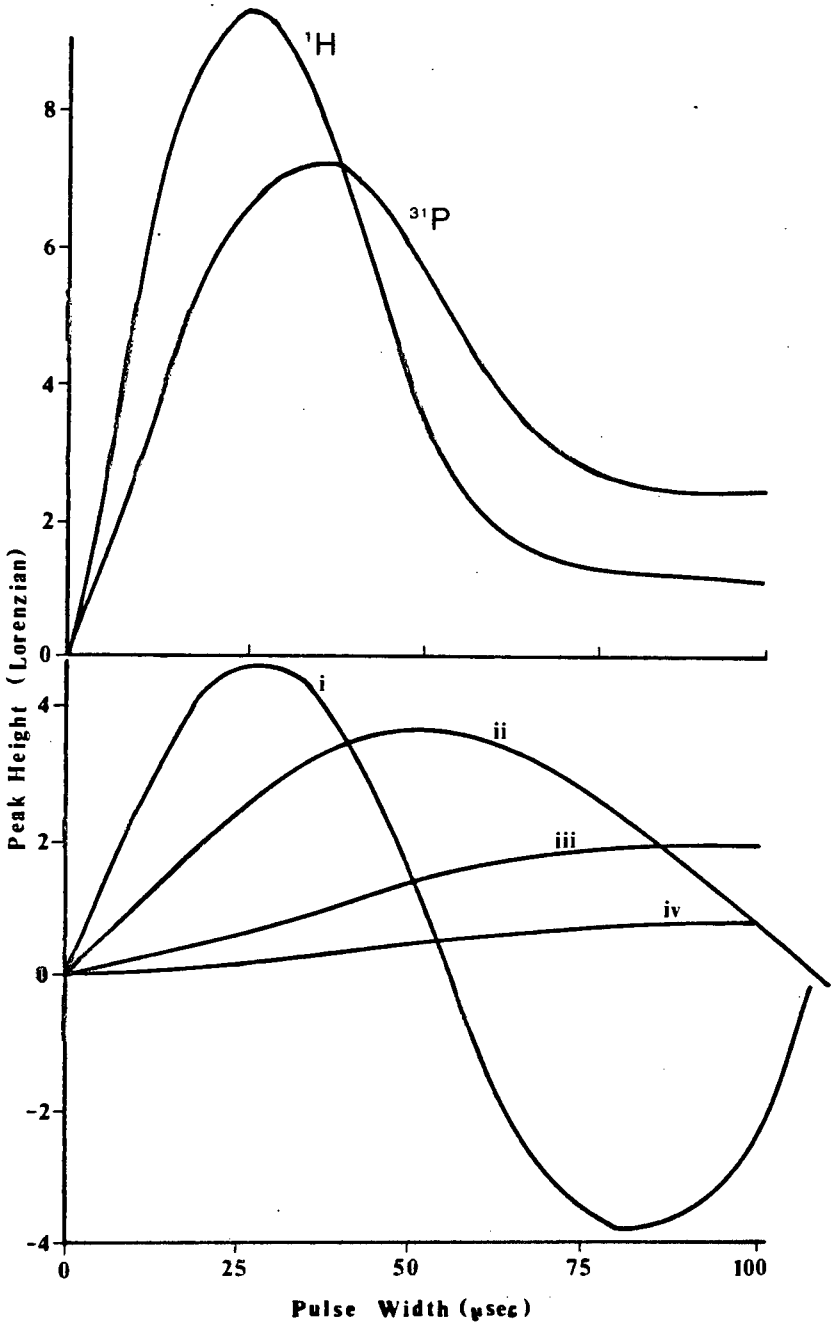

Fig.13 (A) Peak height vs pulse width for ^1H and ^{31}P using prolate elliptical coil; (B) peak height vs pulse width for rows of H_3PO_2 in capillary tube phantom using prolate elliptical coil. Roman numerals correspond to coil planes in Fig.9.

degrees. In addition, the planes further away have reached at most half of their maximum height and will not contribute as much to the resulting spectrum as if the coaxial coil were used. This coil was designed with the specific purpose of rat brain spectra in mind but other coils were found to have higher Q and better signal-to-noise.

(2.7) Depth and Pulse Width in Surface Coils

Fig.14 shows the relationship between 90 degree pulse width and penetration depth into the sample taken from data from the capillary tube and three "point" experiments. Most coils follow the trend which dictates that longer pulse widths are required for excitation of distant regions. The dots represent the pulse width of the maximum peak height shown in Fig.5 for the 90 degree tip angle determination experiment. By interpolation of the "points" in Fig.14, it can be seen that in most cases, this pulse width corresponds to a region of the sample located about r/4 axially away from the coil's plane. The dimensions of the volume of this region may be approximated by the extent of $B_1(xy)$ uniformity shown in Fig.2 (dotted line) and the outer diameter of one capillary tube to give a volume of ca. 10 mm x 10 mm x 3 mm. Perusal of Fig.10 reveals that a ca. 25 μsec pulse width for the flat coil minimizes the signal from the plane of spins closest to the coil but yields an

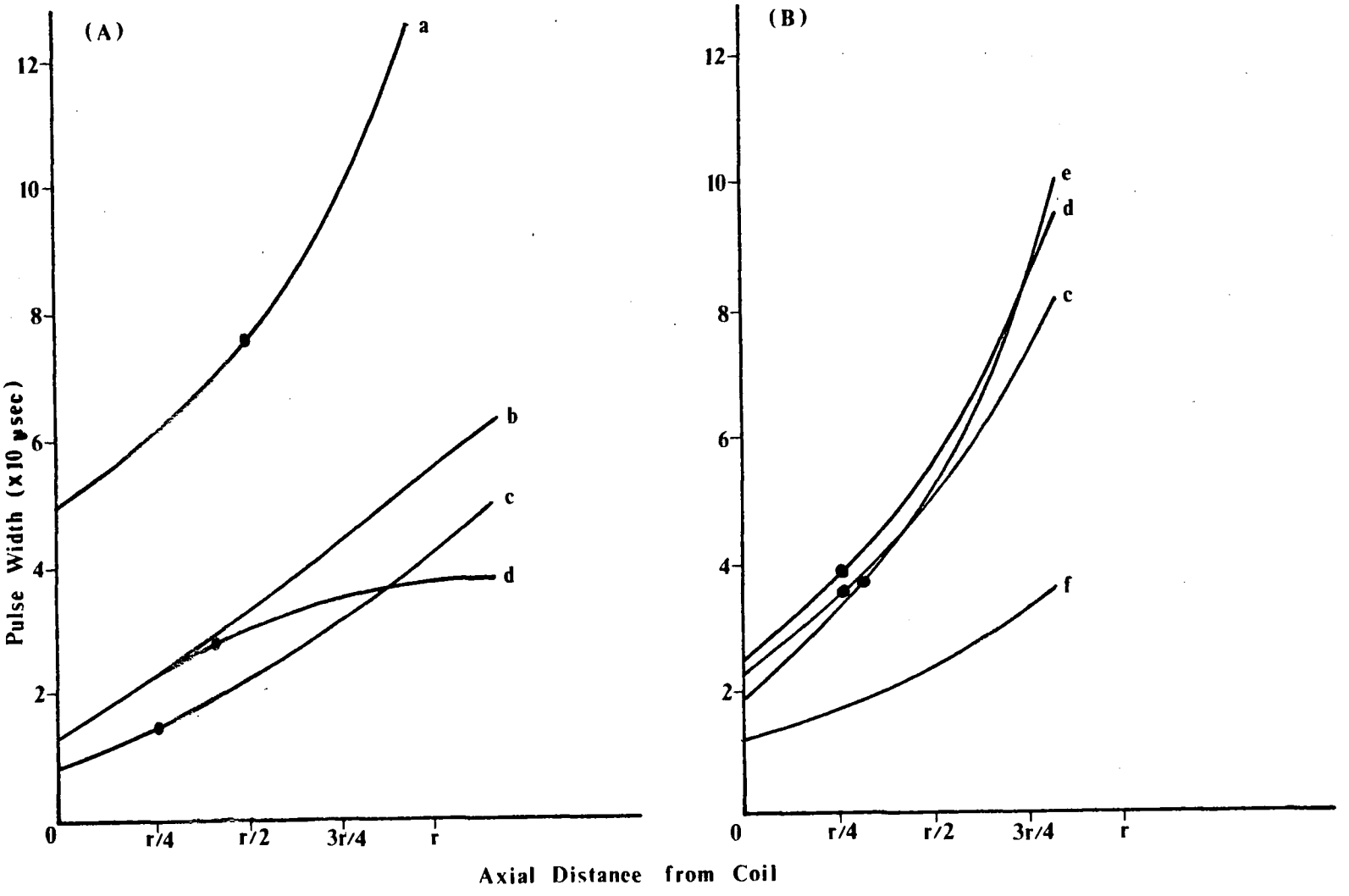

Fig.14 Axial distance and 90 degree pulse width relationship for a variety of surface coils. (A) ^{1}H; (B) ^{31}P; (a) 4.5 cm single turn Cu coil; (b) 2 cm double turn Cu coil; (c) 2 cm flat Ag/Cu coil; (d) 2 cm double turn Ag/Cu coil; (e) prolate ellipse Ag/Cu; (f) oblate ellipse Ag/Cu.

appreciable signal from the next adjacent plane of spins. This pulse width in Fig.14 corresponds to the sample region located ca. r/2 from the coil plane, and is noted in Fig.5 on the curve. In the 90 degree tip angle determination, therefore, the maximum peak height generally corresponds to the sample region ca. r/4 from the coil plane while the pulse width required to excite the sample at r/2 is determined by the efficiency and geometry of the coil. the large (4.5 cm) single turn coil deviated from this trend showing the maximum signal coming from r/2 away. Fig.15 is an expanded view of Fig.14b with data from the 2 cm single turn Ag/Cu and 2 cm Ag/Cu 0.9 surface coils added. The ^{31}P data shows that the slope of the 0.9 coil was the least positive; this coil was the best in separating the greatest intensity signal from each plane of spins in the capillary tube experiment using the smallest pulse widths of all the coils.

The experiment depicted in Fig.16 was done using small vials (I.D. 1.3 cm, O.D. 1.4 cm, length 5 cm). Two vials were taped together and placed on the coil, vertically; one contained ethanol and the other ethyl acetate, both neat. The vial containing ethanol was placed nearest the coil and the spectrum is shown in Fig.16(a). A pulse width of 24 μsec was used so that signals from the region r/2 away would be maximized while minimizing those from the region closer to the coil. The

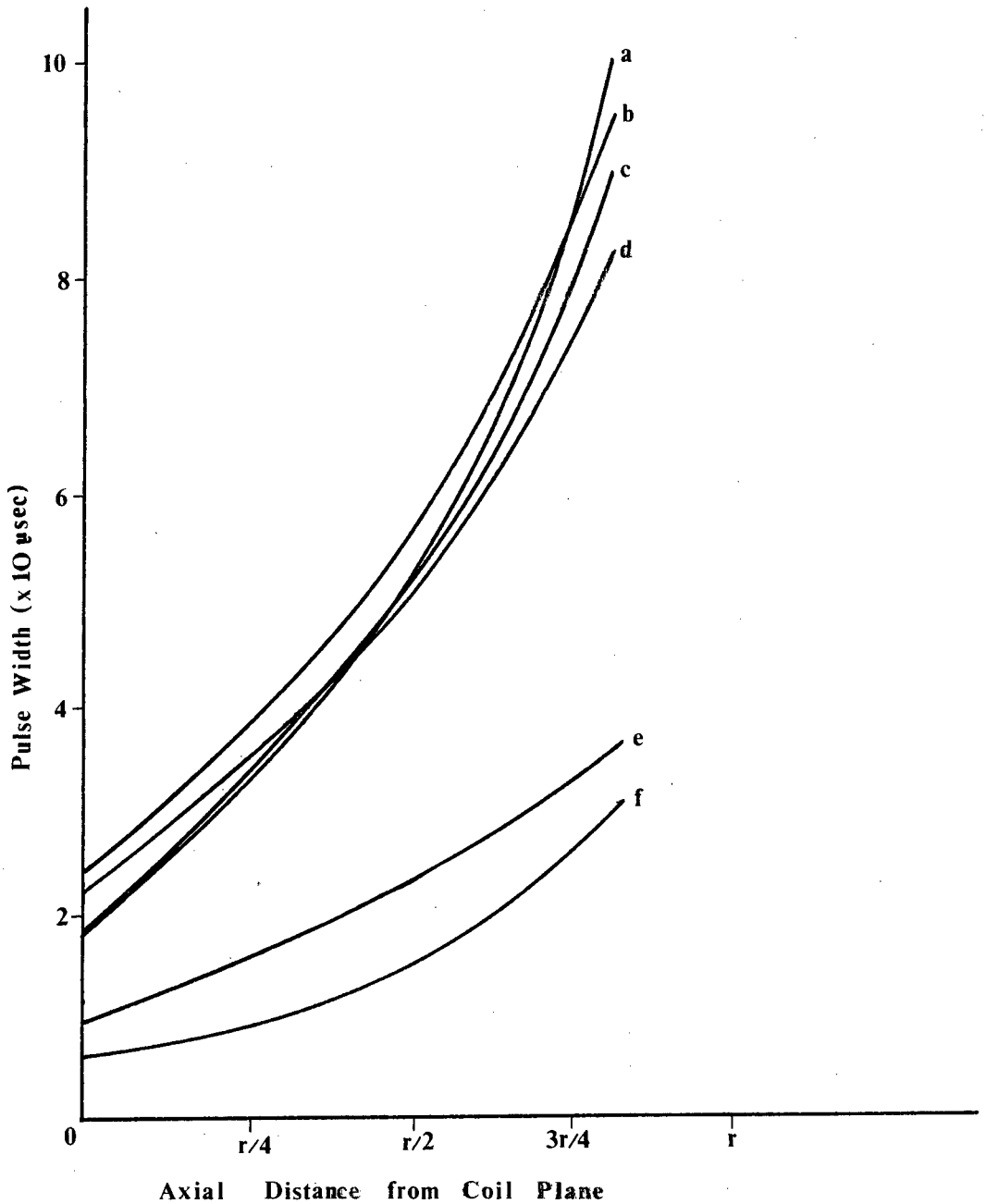

Fig.15 Enlarged version of Fig.14B; (a) prolate ellipse Ag/Cu; (b) 2 cm double turn Ag/Cu; (c) 2 cm single turn Ag/Cu; (d) 2 cm flat Ag/Cu; (e) oblate ellipse Ag/Cu; (f) 0.9 coil Ag/Cu.

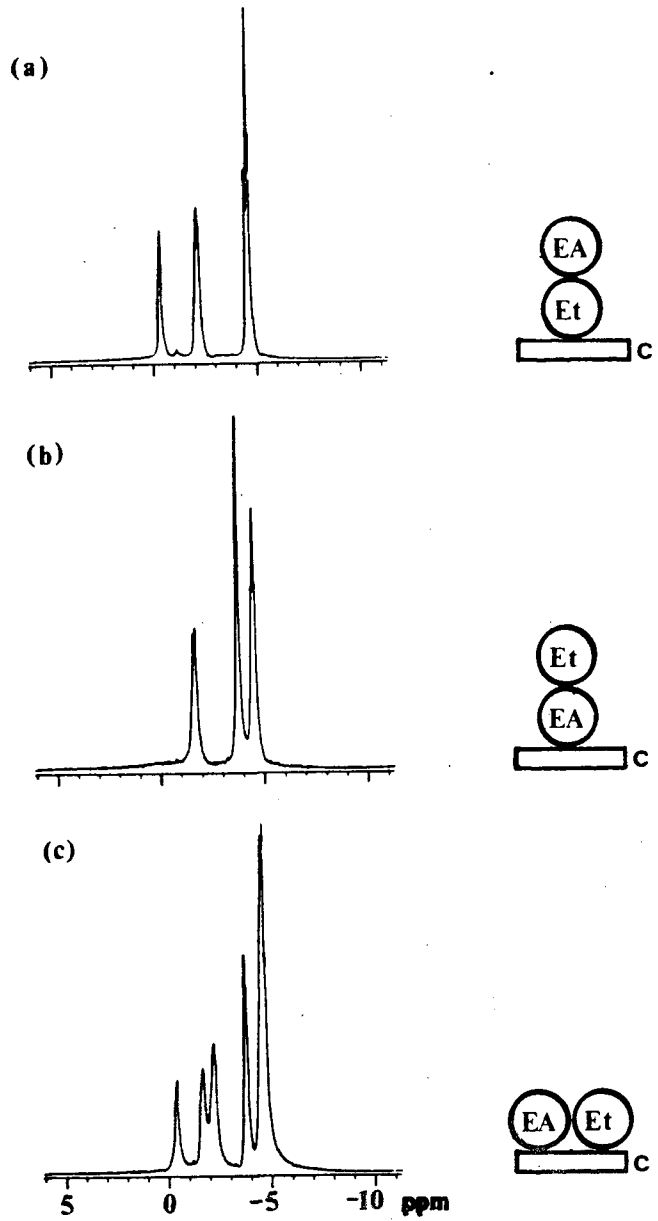

Fig.16 80 MHz ^{1}H spectra from phantom comprised of two adjacent vials (O.D. 1 cm); (a) ethanol (Et) adjacent to the coil (c); (b) ethyl acetate (EA) adjacent to the coil; (c) vials laid flat over the coil. (spectral width=±700.28 Hz; scans=24; block size=2048 points; pulse delay=0.5 sec)

sample was turned over and the experiment repeated. No interference from the upper vial was registered with either spectrum. The sample was then turned flat so that both liquids were within the sensitive volume of the coil. In this case, contributions from both liquids were observed in the resulting spectrum. At 24 μsec, however, the flat coil can experimentally "see" from about 5 to 15 mm axially away, but there was no inteference from the liquid in the upper vial. Even after 100 scans, there was no detectable change in the ethanol spectrum, nor was there any interference when using higher pulse widths. This is to be expected since the liquids are of comparable proton concentration. In the case where the lower vial contained a much less concentrated solution than the upper, interference from the more concentrated solution would likely be observed in spectra where the lower vial was adjacent to the coil.

(2.8) Summary

The flexibility in design of surface coils is an advantage to their use in localization spectroscopy. The size of the sensitive volume of a surface coil is generally determined by the coil's radius but can be slightly influenced in practice by geometry and material used for the coil wire. It is desirable for a coil to have a high Q factor to obtain good signal-to-noise ratios and B_1 fields of higher magnitudes. The tip angles

induced by current passing through surface coils are spatially dependent and vary proportionately with the B_1 field. Generally, short pulse widths excite sample regions lying close to the coil while longer pulse widths induce signals from more distant regions in the sensitive volume. The maximum peak height obtained by exciting a homogeneous sample usually arises from the large concentration of positive tip angles less than 180 degrees in the region r/4 from the coil plane. Specific pulse widths can therefore be used as a crude means of further improving the localizing properties of surface coils. These results are in agreement with theoretical studies previously reported in the literature.[4,23,24]

2.9 Experimental

All spectra were recorded at room temperature using a spectrometer equipped with an Oxford Research Systems (1.89 T), 30 cm horizontal bore magnet and a Nicolet NT-300 console controlled by a Nicolet 1280 computer and 239C pulse programmer operating at 80.3 MHz for ^{1}H and 32.5 MHz for ^{31}P. Samples for NMR spectra were used as neat liquids or solutions prepared analytically by accurately weighing and dissolving in deionized distilled water. The magnetic field gradients were produced by the shim coils using driving voltages generated by digital-to-analogue converters in the 293C unit.

CHAPTER III

IN-VIVO STUDIES USING ^{31}P NMR SPECTROSCOPY

(3.1) Introduction

In-vivo spectroscopy is rapidly approaching the stage where it can be used as a clinical diagnostic tool. In the last two years, there has been a steadily increasing number of papers published on biological applications of spectroscopy, most often using the ^{31}P nucleus. Although the ^{31}P nucleus has only 1/15 the sensitivity of protons, this isotope occurs naturally with 100% abundance, therefore no enrichment is necessary for sample preparation.

The current objective is to characterize metabolism as accurately as possible. Metabolism, considered an important key to understanding diseased states, is a universal process that is chemically identical for all energy processes in humans, and chemically similar between species and even the plant and animal kingdoms. The ten, or so, clearly resolved peaks in a ^{31}P high resolution spectrum comprise a fairly simple manifestation of the metabolic state of an individual. Transitory ailments such as ischemia and chronic conditions such as McArdle's syndrome have already been identified with ^{31}P NMR spectroscopy,[34] and work is currently progressing to lengthen the list of observable disorders.

A phosphorus-31 spectrum of living tissue is a reflection of the fermentation stage of catabolism, the

anaerobic breakdown of biochemical "fuels". The chain of reactions involving transformation of glucose and electron-transfer processes results in the formation of adenosine triphosphate (ATP), the prime energy source for all chemical reactions within the body (see Fig.17). The major participants of the molecular bio-energy cycle are phosphorus containing compounds: ATP, adenosine diphosphate (ADP), phosphocreatine (PCr), inorganic phosphate (Pi), phosphoesters (PE), and sugar phosphates (SP), all of which show narrow resonances, dispersed over a bandwidth of ca. 40 ppm in the relatively simple ^{31}P NMR spectrum. In living tissues, ATP, PCr, and Pi are present at concentrations of at least 0.2mM, sufficiently concentrated for detection by NMR. Many other metabolites and enzyme regulators such as adenosine monophosphate (AMP), phosphoethanolamine (PEA), and 2,3-diphosphoglycerate (2,3-DPG), etc. are present in concentrations of only a few micromolar, or are flowing in blood and are not visible in the spectra, or are hidden under another prominent peak. Changes either in peak height or chemical shift, are regarded as indicative of altered metabolic status. A particularly useful metabolic pointer is the chemical shift of Pi which has been shown to be pH sensitive.[35] Thus, conditions as mild as muscle fatigue and lactic acid build-up have been detected by ^{31}P NMR.[34] Previous to the availability of NMR spectroscopy for *in-vivo* analysis, metabolic studies

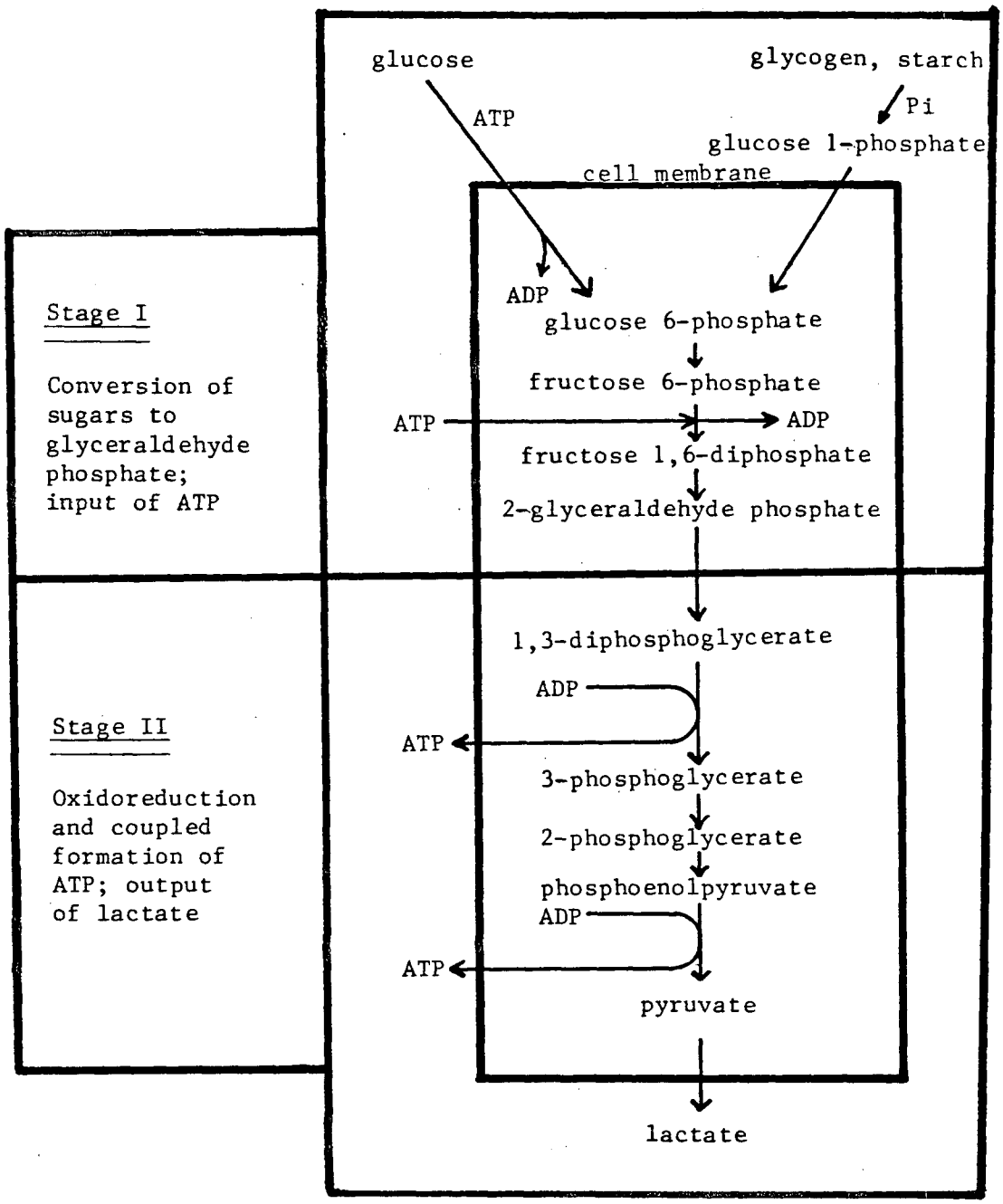

Fig.17 Selected steps of the glycolytic pathway.

of the brain were formidably difficult because of the problems associated with techniques such as perfusion and freeze-extraction.[36] Clearly observable NMR parameters, such as those mentioned above, have encouraged much research in the area of diagnostic spectroscopy. So far, most NMR spectroscopic studies of *in-vivo* systems have required the subject to be small (to fit into the bore of the magnet), mammalian (for comparison with humans), and easily anaesthetized. For these reasons rats have been the most commonly used animals, but gerbils, guinea pigs, cats and dogs have also played roles in NMR experiments. The underlying objective of such studies has been to learn more about human physiological processes, particularly of the brain; similarities between human and other mammalian brains, and ethical considerations, make animal models a valid and convenient choice for experimental specimens.

This chapter presents the results of experiments intended to elucidate and characterize metabolic changes in rat tissues. Preliminary tests *in-vitro* on phantoms which mimic physiological systems were performed to identify various metabolites by their chemical shift. These data are presented first; the *in-vivo* results and discussion thereof follow afterwards.

(3.2) Surface Coil for *In-vivo* Experiments

The objective of the work detailed in Chapter II was to elucidate the properties of some surface coils and find the best one suited for *in-vivo* spectroscopy. The ease with which surface coils can be shaped to the geometry and size of the sample is an advantage. However, the elliptical coil, which was better suited to the shape of a rat's head, had lower Q and signal-to-noise measurements than the 0.9 coil. This latter coil was made with thicker wire which enhances coil sensitivity, albeit that it does not perform as well as thinner wire in terms of achieving high resolution.[36] In the present study, in which it was more important to observe gross changes in the spectra rather than very highly resolved peaks, the combination of the thick wire and linear B_1 gradient was judged to be the most suitable for the envisaged experiments. All the *in-vivo* experiments were made using the single tuned probe.

The vial experiment depicted in Fig.12 showed that the major contribution to spectra emanated from the region of sample which occupied the sensitive volume of the coil. The sensitive volume for most circular surface coils is the hemisphere subtended by a line which originates at the coil center, the length of which is the coil's radius. The 0.9 coil had a diameter of 2.3 cm, making its sensitive volume extend to approximately 1.1

cm from the coil plane. On average, the head of a 300 g rat is ca. 2.0 cm wide, but the brain itself is only ca. 1.2 cm wide including left and right lobes. The jaw and skull of a rat are connected with ligaments, and animated by the massetter muscle which is ca. 4 mm thick and located just below the ear and which effectively shields the brain from the side. With the measurement mode used here, the sensitive volume extends into the brain by ca. 7 mm, meaning that only one side of the brain is sampled. This is ideally suited to the objective of the planned experiment since differences between the respective sides of the brain were of interest.

(3.3) *In-Vivo* Experiments

(a) Background Information

In this section, some *in-vivo* ^{31}P NMR experiments will be discussed. The choice of phosphorus-31 as the nucleus of interest is suited to the study of metabolism since most of the molecules containing phosphorus in mammals are involved in energy exchange. Before embarking on the actual experimental results, it is instructive first to discuss some of the biochemical reactions which are being observed via NMR.

Animals build up and break down energy-stores by processes called anabolism and catabolism, which are akin to photosynthesis and respiration in plants. Storage of

energy in mammals is accomplished via digestion and absorption of foods. Energy needed to do biochemical work is obtained through the glycolytic pathway, which is the process by which glucose is utilized as an energy source with lactate produced as a by-product. The major constituents of the glycolytic pathway are shown in Fig.17[37]. The substrates enclosed in the inset partake in reactions within the cell whereas the others are present in the intercellular spaces. Fig.18[37] is a schematic representation of the mechanism of the ATP-ADP system. Biochemical energy processes of mammals are economically designed to obtain the maximum output with the mimimum input. Hence high energy compounds are usually coupled *indirectly* to low energy compounds to effect a transfer of a large amount of energy with little lost to the system. The universal currency for all *in-vivo* biochemistry is ATP; it is used to build energy-reserve compounds and is expended in energy requiring reactions. There are very few biochemicals which have greater phosphate leaving potential than ATP. Phosphoenolpyruvate (PEP) is one of these compounds and is listed in Fig.18[37]. In order to produce glucose-6-phosphate, PEP loses one phosphate group to become pyruvate and ATP:

$$\text{PEP} + \text{ADP} \rightleftharpoons \text{pyruvate} + \text{ATP}$$

The ATP then combines with glucose to yield glucose-6-phosphate:

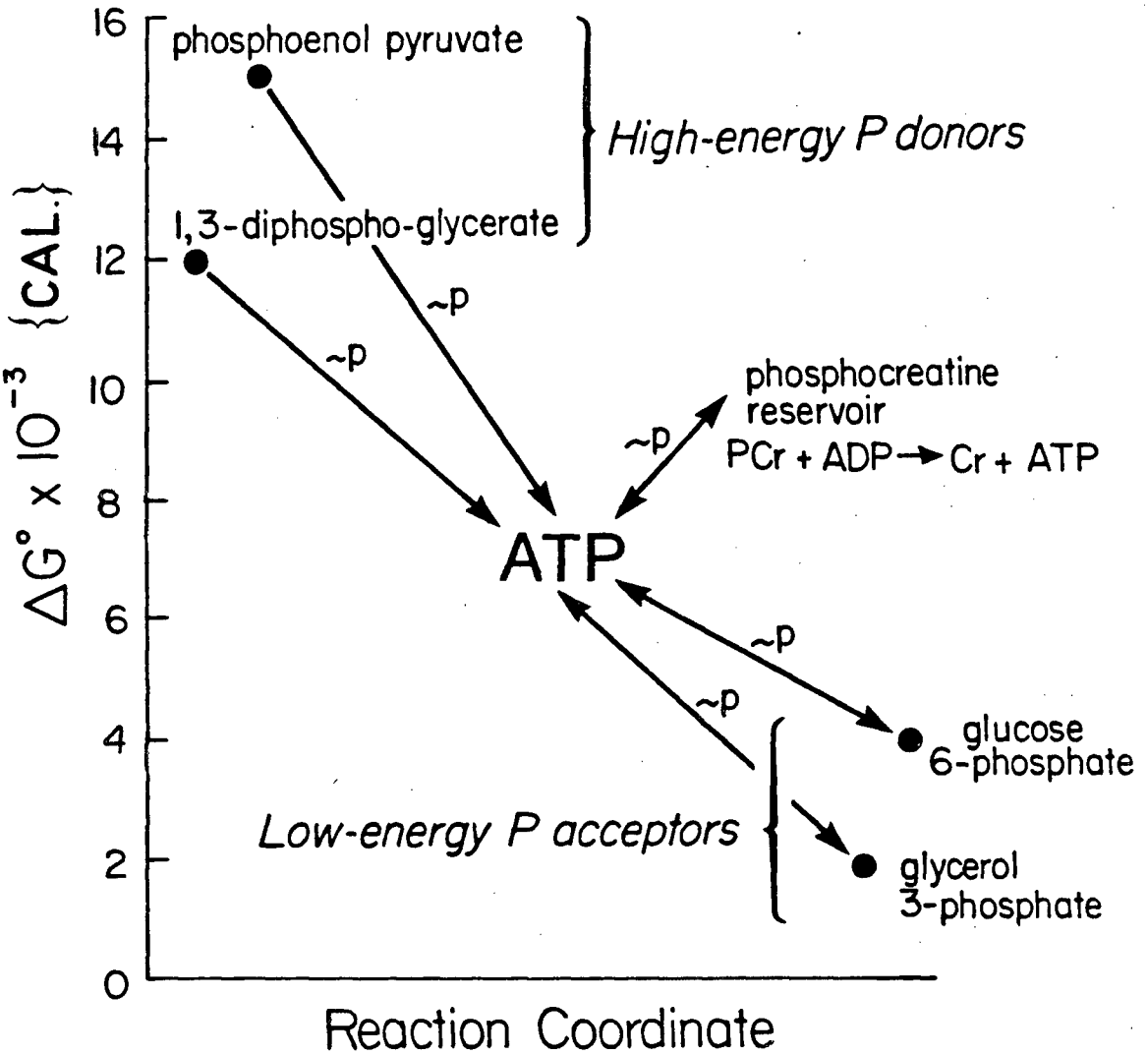

Fig.18 Energetics of phosphate exchange reactions of metabolism.

$$\text{glucose} + \text{ATP} \rightleftharpoons \text{glucose-6-phosphate} + \text{ADP}$$

In this way a high energy phosphate donor, (PEP), is coupled to a low energy phosphate acceptor, (G6P), without large amounts of energy being expended and absorbed in one step and the system does not stray far from thermal equilibrium. In fact, evidence suggests[37] that all biochemical processes act in this way with ATP and ADP as the mediators in the energy cycle.

In the background of all this biochemical activity, lies an energy reservoir where high energy phosphates are stored in compounds called phosphagens. The major phosphagen in vertebrates is phosphocreatine; this is used for storing metabolic potential in the form of phosphate bond energy. PCr is another molecule with a higher phosphate leaving potential than ATP and is formed by the addition of a phosphate group to creatine:

$$\text{PCr} + \text{ADP} \rightleftharpoons \text{creatine} + \text{ATP}$$

where the equilibrium lies to the right. The reaction above is of prime importance in muscular contraction when PCr is used to create large amounts of ATP. The amount of ATP in muscle actually remains fairly constant during muscle-contraction until the PCr level is depleted. It has sometimes been found, that more ATP was used by the muscle than was present in the cell before the

contraction.[38]

In the present studies, two different barbiturates were used to anaesthetize the rats: Pentabarbitol, which is widely used for short-term studies, and inactin, for long-term measurements; both injected interperitoneally by syringe. The short-term anaesthetic was suitable for ca. 45 minutes whereas the long-term one lasted ca. 48 hours. The only visible effects on the rat were slower breathing and general muscular relaxation which would be expected in an unconscious (sleeping) state.

(b) *In-vitro* References

In spite of ample studies in the literature, prior to any *in-vivo* spectroscopic measurements, it was deemed necessary to identify the expected resonances by their chemical shifts. Solutions of various physiological metabolites were prepared analytically *in-vitro*, and titrated to neutral pH. ^{31}P spectra were obtained from mixtures of these solutions using the same surface coil as for the *in-vivo* work. It is important to note that an internal standard, PCr, was used as the zero of the abcissa of the spectra and all chemical shifts were measured relative to it. This corrects drifting of the peaks due to small differences of the shim settings in the magnet. Recording these spectra facilitated further identification of peaks in *in-vivo* spectra by comparison

of chemical shifts.

Table II lists the metabolites which appear clearly in a ^{31}P spectrum of living tissue, along with their molecular structure and NMR spectrum. Spectra of various mixtures follow in Fig.19. In the course of the breakdown of glucose, phosphorus containing moieties are created, each of which can theoretically be found in a ^{31}P NMR spectrum. However, since chemical shifts are dependent on molecular structure and electronic shielding, some of the compounds shown in Table I and Fig. 19 differ only slightly in chemical shift and may be difficult to distinguish in a spectrum. Perusal of the selection of compounds in Table II indicates that some resonances may be hidden by other stronger signals. Information about these substances, such as c-AMP and o-phosphoethanolamine, for example, will be more difficult to extract for this reason. The limitations of ^{31}P spectroscopy in view of this fact will be discussed later. Generally it should be noted that ester phosphates and inorganic phosphate appear downfield from phosphocreatine and nucleoside phosphates appear upfield. Phosphoric acid would appear downfield from PCr were it present as well. Exact chemical shifts recorded for various phosphorus containing metabolites[36] have been obtained *in-vitro* and can act as a guide for peak assignments.

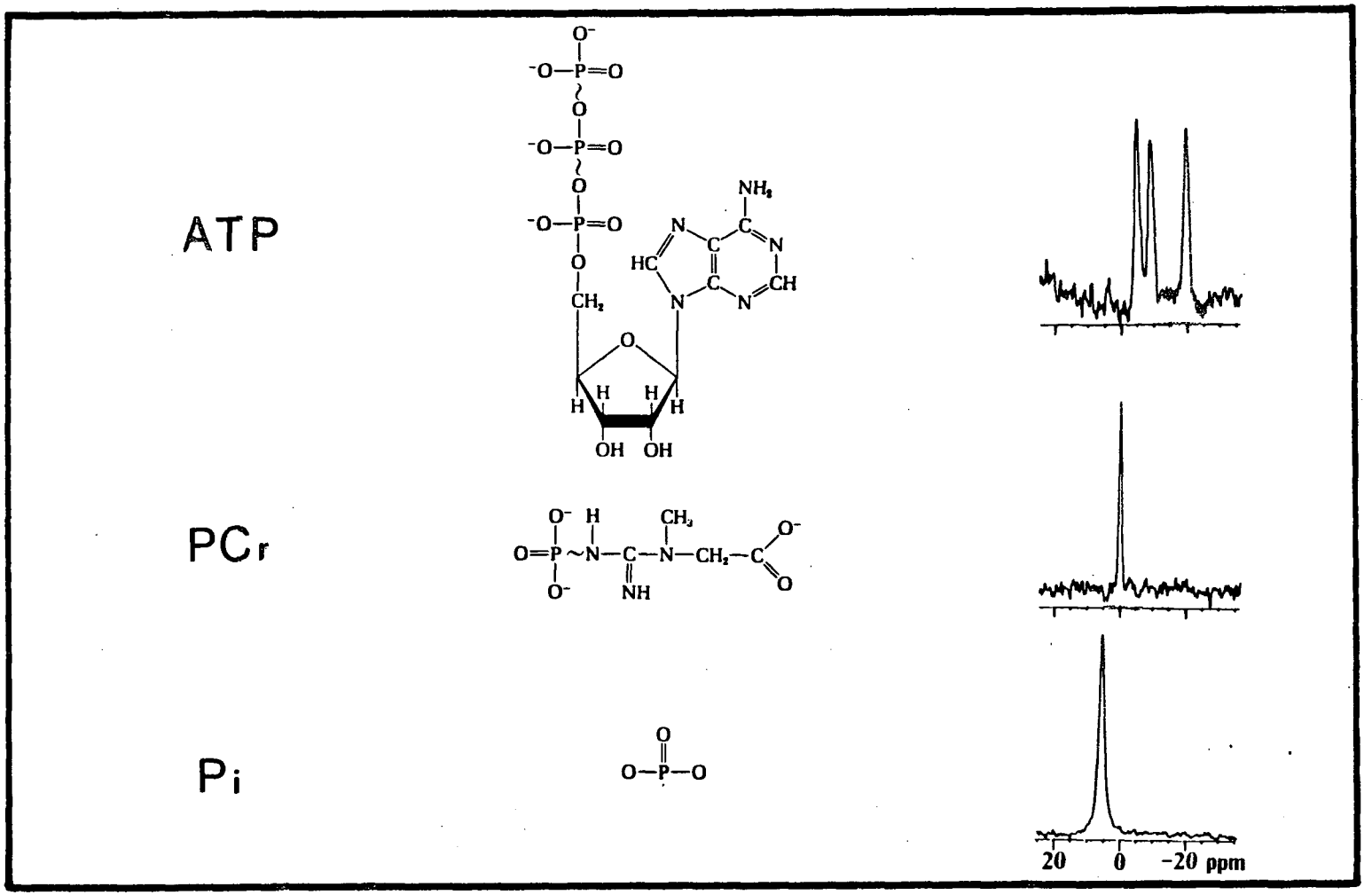

Table II Molecular structure and ^{31}P NMR spectra of selected phosphorus-containing metabolites.

c-AMP

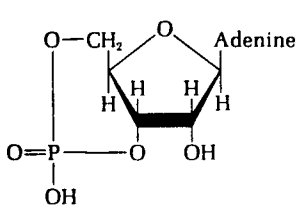

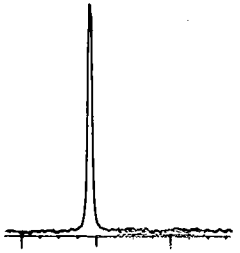

PEA

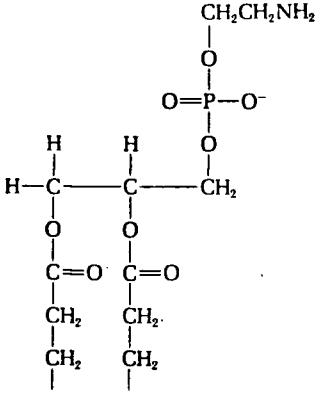

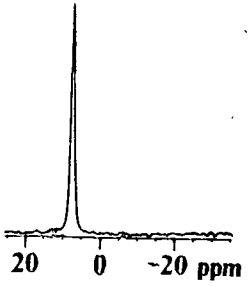

PEP

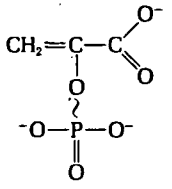

Table II Molecular structure and ^{31}P NMR spectra of selected phosphorus-containing metabolites.(cont'd)

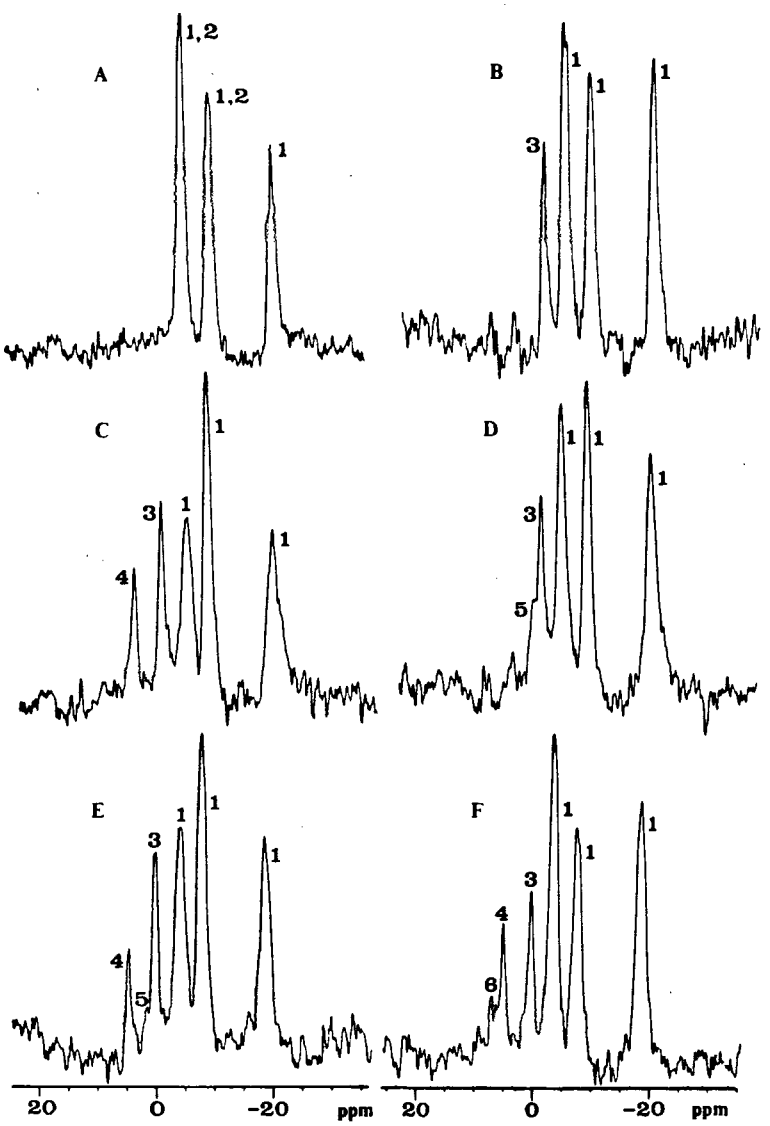

Fig.19 In-vitro ^{31}P spectra of various mixtures of metabolites at pH=7; (A) ATP + ADP; (B) ATP + PCr; (C) ATP + PCr + Pi; (D) ATP + PCr + c-AMP; (E) ATP + PCr + c-AMP + Pi; (F) ATP + PCr + o-PEA + Pi; (1) 30 mM ATP; (2) 25 mM ADP; (3) 41 mM PCr; (4) 25 mM Pi; (5) 0.5 M c-AMP; (6) 0.5 M o-PEA; using 2 cm 0.9 Ag/Cu coil. (spectral width=±1000 Hz; scans=200; block size=2048 points; pulse delay=2 sec; line broadening=10 Hz)

(c) *In-Vivo* Muscle Spectra

Muscle tissue is understandably of interest in applications of ^{31}P NMR since large amounts of energy are used in animating a skeleton. The biochemical energy pathway can easily be tapped with muscle as well. Human subjects may be asked to exercise an arm or leg prior to obtaining spectra or rat muscle can artificially be made ischemic.

Fig.20(b) shows a ^{31}P spectrum of a leg of an anaesthetized (inactin) rat. Metabolites clearly visible in the spectrum are PCr, ATP, Pi, and sugar phosphates. PCr and ATP are present in ca. 20 mM and 5-10 mM concentrations respectively. The ATP peaks are all of similar height and linewidth; ADP is presumably buried under these resonances. The lack of a signal from 2,3-diphosphoglycerate in muscle indicates that blood and skin phosphates do not contribute significantly to the spectrum.[36] Fig.20(a) is a ^{31}P spectrum of a human arm shown to illustrate the universal characteristics of vertebrate muscle metabolism. Differences in signal-to-noise and number of acquisitions between the two spectra are due to improvements in coil and probe design which occurred inbetween recording these spectra.

The method adopted for characterizing spectra as muscle or brain tissue was to measure the PCr/βATP peak height ratio.[4] These two peaks have been chosen since

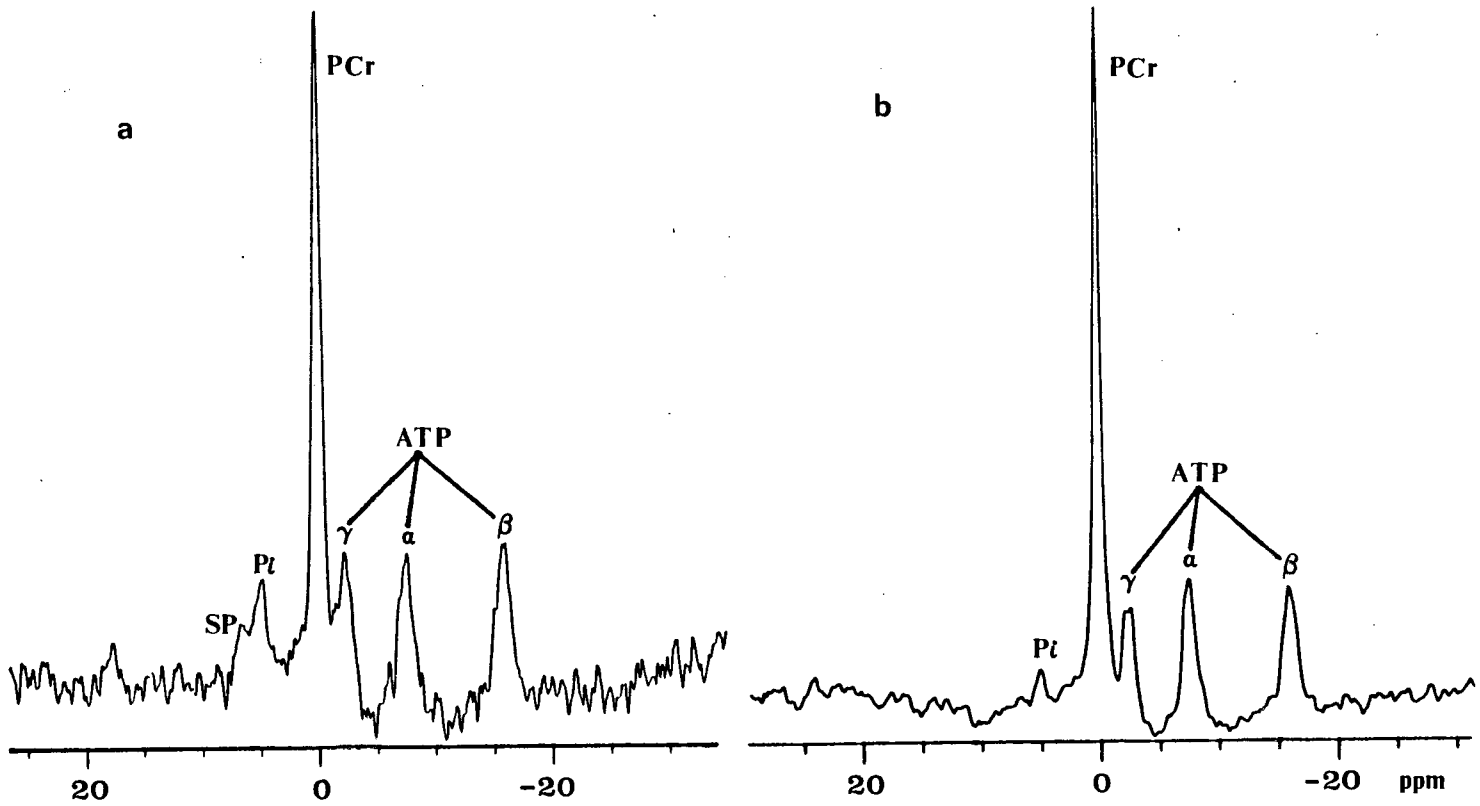

Fig.20 ^{31}P NMR *in-vivo* spectra of (a) human arm; (b) rat leg; using 2 cm 0.9 Ag/Cu coil. [Human arm(using 2 cm double turn Cu coil): pulse width=38 μsec; scans=400; block size=1024 points; line broadening=8 Hz; Rat leg(using 2 cm 0.9 Ag/Cu coil): pulse width=12 μsec; scans=200; block size=2048 points; line broadening=10 Hz; both spectra: spectral width=±1000 Hz; pulse delay=2 sec]

they arise as resonances from a single source rather than a combination of signals. Muscle spectra generally have a PCr/βATP ratio of ca. 4:1.

In order to observe a different state of metabolism, an elastic was placed around the rat's leg just below the hip joint to restrict the flow of blood to and from the leg. Experiments such as this have previously been reported in the literature[4,36] but were undertaken here as a verification of the method and equipment used. Spectra were acquired every ca. 4 minutes for about 1.5 hours after which the elastic was removed, with spectra continuing to be recorded for another 40 minutes. Results are shown in Fig.21. During the interval when the rat's leg became increasingly ischemic, it can be clearly seen that the phosphocreatine is being depeleted with the concommitant increase of inorganic phosphate. The steady state levels of ATP in these spectra suggest that PCr played a major role as a source of phosphate energy, contrary to what would normally be expected. This experiment, however, is a manifestation of the effects of abnormal stress on muscle tissue, as opposed to the effects of moderate exercise. A closer look at Fig.21(d)-(e) suggests that there may be a limit below which the energy stores of PCr will not fall. During this period of the experiment, the level of PCr remained virtually constant. A striking feature of this set of spectra is the rapidity with which PCr is restored after

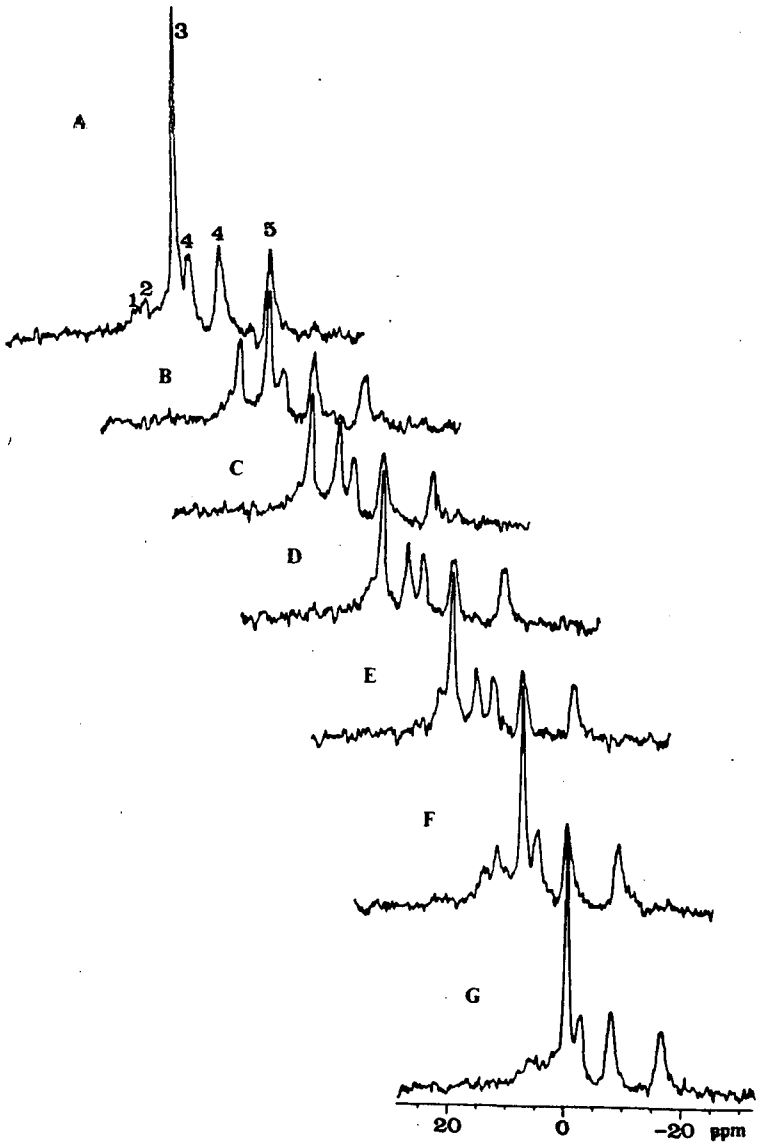

Fig.21 ^{31}P NMR *in-vivo* spectra of artificially induced ischemia in a rat leg using 2 cm 0.9 coil; (1) SP; (2) Pi; (3) PCr; (4) ATP/ADP; (5) ATP; (A) prior to insult; (B) after 20 min; (C) after 44 min; (D) after 64 min; (E) after 84 min; (F) 5 min after circulation restored; (G) 30 minutes after circulation restored; using 2 cm 0.9 Ag/Cu coil. (spectral width=±1000 Hz; scans=200; block size=2048 points; pulse width=12 μsec; pulse delay=1 sec; line broadening=10 Hz)

removal of the elastic obstruction. Within 5 minutes of the return of blood circulation to the rat's leg, PCr had been virtually restored to it's original height.

Exercising a human forearm yields similar results to the above experiment, though not as dramatic. An increase of inorganic phosphate without any effect on PCr is the usual observation when the muscle remains oxygenated. Under anaerobic conditions, a decrease in muscle pH, and borrowing from PCr energy reserves prevails.

(d) *In-Vivo* **Brain Spectra**

Skeletal muscle is a choice subject for ^{31}P NMR spectra because it is easily accessed and shows detectable concentrations of phosphorus containing metabolites. However, brain metabolism, being of primary interest here was the object of further experimentation. The first ^{31}P *in-vivo* rat brain spectrum was published in 4980[1] and since then, a handful of fruitful experiments have appeared in the literature.[39-42] The choice of rats follows standard physiological practices since they can be used as models for human brain processes, are very resistant to disease and are easily bred under controlled conditions. Physiological insults applied to rat brain tissues can act as models for human diseases, the causes and potential cures of which remain unknown.

A typical ^{31}P *in-vivo* spectrum of rat brain is shown in Fig.22. Despite small variations in peak height and shape between animals, this spectrum can be considered as a generic rat brain spectrum. Features appearing here which are common to muscle tissue are the ATP, PCr, Pi and sugar phosphate peaks, the latter being more prominent here. There is also the appearance of a resonance at ca. 2.5 ppm which is likely phosphoenolpyruvate. The inorganic phosphate resonance at ca. 5 ppm is partially obscured by the 2-phosphate of 2,3-DPG in blood.[36] This interference does not occur in muscle spectra. Elevations in brain phosphodiester levels may be associated with this fairly mobile substituent of myelin, the protein coating on neural axons. Elevations in brain sugar phosphates may be due to greater brain energy demands supplied via glycolysis.[22]

A subtle but useful characteristic of brain spectra such as this is the reduced PCr/βATP ratio as compared with muscle spectra. In brain this quantity is reduced to 5:2 (cf. muscle spectra: 4:1) as a consequence of the intrinsically longer T_1 of PCr in brain compared to muscle.[22] In addition, there is a broad resonance superimposed on the spectrum which arises from the immobile phosphates in the bone of the skull. Prior to obtaining this and other spectra, rat brain spectra were obtained by laying the rat supinely over the surface coil. This resulted in a much larger hump which could be

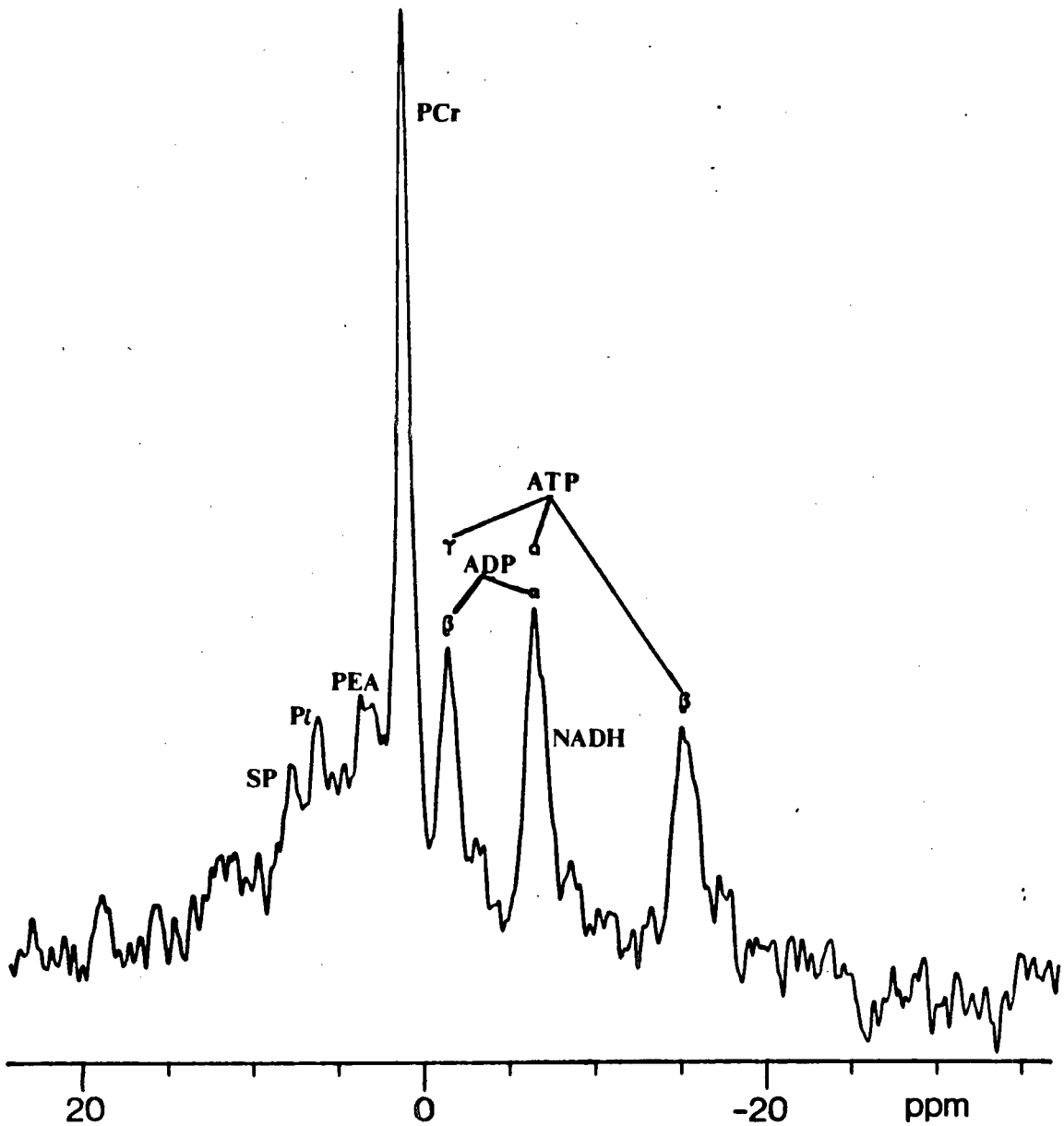

Fig.22 ^{31}P NMR *in-vivo* spectrum of rat brain; using 2 cm flat Ag/Cu coil. (spectral width=±1000 Hz; scans=600; block size=2048 points; pulse width=24 μsec; pulse delay=2.5 sec; line broadening=10 Hz)

partially removed by convolution difference.[4,43,44] This problem was somewhat alleviated both by removing the first point of the FID during data processing, or placing the surface coil on the side of the rat's head and thus avoiding a "shield" of bone. Instead the obstruction encountered here was the massetter muscle, the muscle connecting the jaw to the skull. Though interference would be the same on both sides of the head, removal of the massetter muscle indicated that its contribution to the spectra was negligible.

In an effort to observe differences in brain metabolism, a preliminary test was used to establish the sensitivity of NMR to brain tissue. After acquiring a spectrum of a normal rat's brain, the rat was subsequently sacrificed with an overdose of barbiturate. Another spectrum was then acquired of the deceased rat's brain. Spectra are shown in Fig. 23. The objective here was to determine whether a study of brain disease would be feasible via NMR. If ^{31}P NMR was not sensitive enough to show a difference for the most dramatic metabolic change of all, it certainly could not be used to detect more subtle deviations from normal metabolism.

The deceased rat brain spectrum has some characteristic features which correspond to the biochemical understanding of death. In this case, "death" refers to the fifteen minute period following the

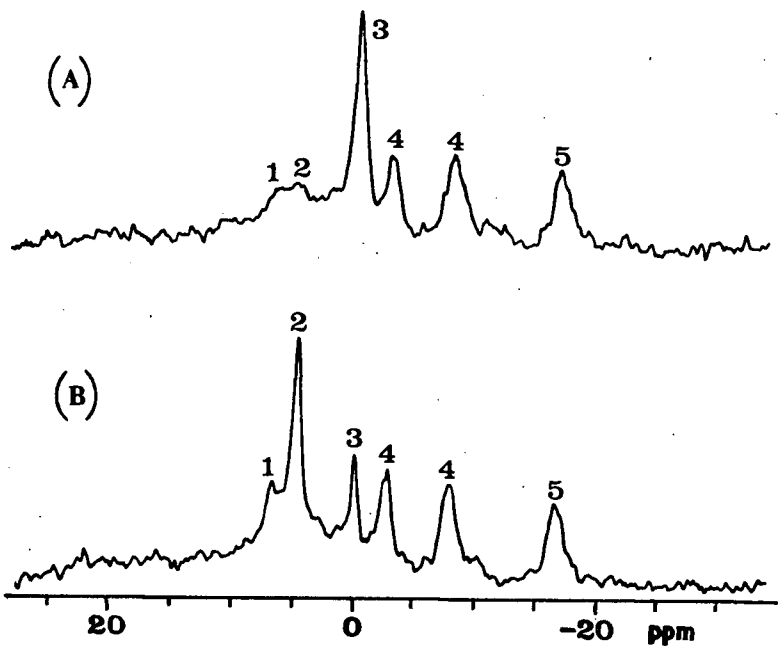

Fig.23 ^{31}P NMR *in-vivo* spectrum of rat brain; (A) live rat; (B) deceased rat; (1) monosugar phosphates; (2) Pi; (3) PCr; (4) ATP/ADP; (5) ATP; using 2 cm 0.9 Ag/Cu coil. (spectral width=±1000 Hz; scans=200; block size=2048 points; pulse width=12 μsec; pulse delay=1 sec; line broadening=10 Hz)

cessation of the heart beat. The large inorganic phosphate peak and small PCr peak indicate that catabolism is proceeding to completion. The residual signal from PCr gives further evidence that much phosphate bond energy has been expended with the resulting build-up of Pi at the expense of all other phosphate donor molecules. The fact that PCr yields a signal at all in the spectrum indicates that a small remainder of the phosphagen is left over, similar to the case of the ischemic rat leg (Fig.21). Peak shapes for ATP/ADP eventually broaden and lose resolution with time, suggesting some instability or decomposition of these metabolites. With spectral identification of live vs deceased metabolic states, it was possible to proceed to an examination of a rat model for human brain disease.

In an effort to observe the effects of mildly altered metabolism in the brain, a physiological insult was artificially applied to achieve this. The procedure involved the injection of kainic acid (I) into one side of a rat's brain. Kainic acid, an extremely potent neurotoxin, was used for its deleterious effects on the brain which are similar to those caused by Alzheimer's disease in humans. Many efforts to elucidate the characteristics and causes of Alzheimer's disease, or Huntington's Chorea, utilize kainic acid treatments as models for these conditions. Injecting one side of the brain allowed the other lobe to be used as a control;

biologically, this procedure is more reliable than comparing one animal to another since there is a large standard deviation for "normal" characteristics and every rat brain is simultaneously similar yet unique.

Kainic acid (KA) is an ingredient of the seaweed *Digenea Simplex* which grows off the coast of Japan. First isolated in 1953 by Takemoto and his colleagues,[45] it was shown to have anthelmintic and in some cases emetic properties but its effect on mammalian neurons was unknown until later. However, it was known that L-glutamate (II) was a strong excitant of neurons in various parts of the central nervous system, hence KA (I) which is a disubstituted derivative of glutamate, was suspected of showing similar or opposite behavior. Unlike glutamate, however, kainic acid is a heterocyclic molecule.

(I)

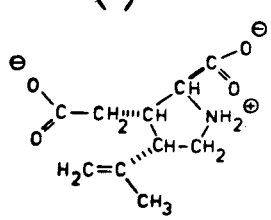

kainate

(II)

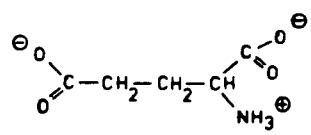

glutamate

Kainic acid is highly neurotoxic due to its ability to cause sustained cell depolarization, and concommitant increase in neural membrane permeability.[45] Essentially, KA kills neurons by exciting them to death. Of the substituted glutamates recognized as excitotoxic, KA is the most potent and long acting in the mammalian central nervous system. The exact mechanism by which the acid operates is still unknown, although some theories have been advanced. What is known, however, is that kainic acid, like glutamate, is selectively toxic. It can kill only neurons whose cell bodies lie in the vicinity of the injection but cannot penetrate axons or dendrites of other nerve cells terminating or passing through this region (see Fig.24). In this way, KA has been used as a highly specific lesioning agent since the damage it does is localized to a given brain volume. However, some neurons are relatively resistant to KA and a few are even completely unaffected.

The usual dose given to a rat was from 2 to 10 nanomoles in a volume of up to a few microlitres. Large doses of KA are superfluous since the activity of the nerve synapses is virtually arrested after a dose of 15 nanomoles.[45] The experimental rat was injected with 5 nmoles and left to rest for one week while the acid acted on the brain tissue. ^{31}P NMR spectra were then acquired from both sides of the rat's head after anaesthetizing the rat with inactin. The spectra are shown in Fig. 25.

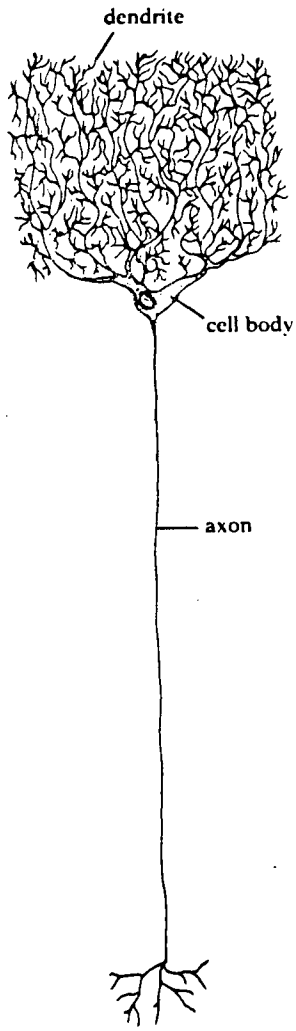

Fig.24 Schematic drawing of a brain neuron. Dendrite fibres are usually profusedly branched to bring much information to the cell body. The long thin axon carries information away from the cell body. Kainic acid can diffuse across only the cell body membrane, but cannot penetrate axons or dendrites.

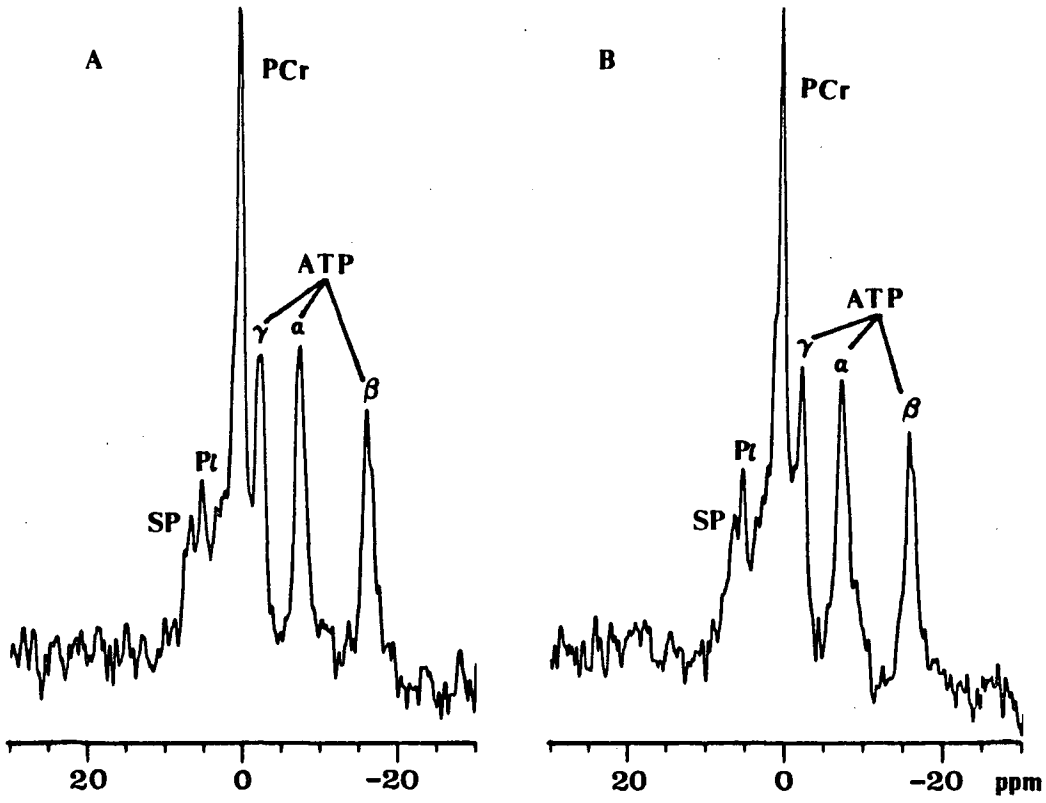

Fig.25 ^{31}P NMR *in-vivo* spectrum of lesioned rat brain; (A) right brain; (B) left brain; using 2 cm 0.9 Ag/Cu coil. (spectral width=±1000 Hz; scans=200; block size=2048 points; pulse width=12 μsec; pulse delay=1 sec; line broadening=10 Hz)

Within the range of standard deviation expected for a spectrum of living tissue, it is not possible to differentiate these spectra by any distinguishing features. The many spectra acquired from any one side of the head show as much variation in peak height and resolution as do these two. The significance of this is manifold. It may suggest that the dosage applied to the brain was not enough to generate a detectable change via NMR. A concentration of 5 nanomoles in a few microlitres may be significant and measurable with fine neurochemical devices but would not exceed the minimum limit of sensitivity of NMR. Thus a larger or more pervasive insult may be required. Another possibility is that the action of KA does nothing to alter the phosphorus containing metabolites within the cell. Since KA interacts at synapses, it may only be involved in debilitating neurotransmitters or changing the physical structure of the receptor sites of neurons. In this case no change in the ^{31}P spectrum would be expected, though in terms of concentration, this conclusion could not be assumed based on the dosage given, since the overwhelming concentration of phosphorus metabolites in the rest of the brain (same side) would obliterate the appearance of this effect in the spectrum. Further attempts to "saturate" the rat brain with KA or to make multiple lesions simply led to the death of the animal. A potential adjunct to this experiment might be to further

inject the rat with an enzyme or phosphorus-containing metabolite to observe whether a specific step in the glycolytic pathway has been blocked. In addition to this, once reliable water suppression techniques are established, ^1H spectra of each side of a lesioned rat brain may yield more fruitful results since proton resonances from neurotransmitters can be traced. In consideration of the various explanations for observing statistically similar spectra for a diseased and normal brain, further attempts at characterizing this condition via NMR may not yield more illuminating results. In addition, the effect of the anaesthetics has not been considered as a separate entity in itself. By their very nature, anaesthetics operate by affecting metabolism and a study on their precise effects is desirable. Unfortunately, problems associated with obtaining NMR spectra from stationary samples precluded acquisition of spectra from unanaesthetized rats. It is not known then, whether the effect of the anaesthetic on metabolism would also mask the action of kainic acid on brain tissue. These questions beg for attention from further experimentation with NMR and animal models.

3.4 Experimental

The spectrometer and magnet used for these experiments were described in section 2.9. Solutions were made analytically by weighing accurately and dissolving

in deionized distilled water; pH was adjusted by titrating with dilute HCl and NaOH; the appropriate aliquots were pipetted into the sample container.

Male Wistar rats (250-350 gm) were used for all *in-vivo* experiments except the human arm experiment for which a volunteer was employed. Anaesthetics were prepared in concentrations of 5 gm % (pentabarbitol), and 10 gm % (inactin) and dosages for both were given at 0.1 ml/100 gm body weight. Injections were made interperitoneally by syringe.

Shimming on rat heads was accomplished by changing the transmitter frequency and preamplifier to ^{1}H while the probe was kept tuned to ^{31}P.[46]

CONCLUSION

The work presented in this thesis was undertaken in an effort to bridge the chasm which separated the objectives of localization spectroscopy from its present sundry applications. To this end, the properties of surface coils have been studied to provide justification for their use. After elucidating some of the advantages and disadvantages of surface coils, a coil was chosen with optimal geometry and the most suitable wire for the application intended. *In-vivo* examinations of the metabolic status of rat muscle and brain were performed with a surface coil using the phosphorus-31 nucleus as a probe. Some conclusions and directives will now be presented in view of these and other results in the literature.

It has been observed that the most notable characteristic of surface coils, namely the nonuniform B_1 field, is what makes further localized spectroscopy possible. Differences in peak amplitude modulation frequency within the sensitive volume of the surface coil allow the experimentor to use predetermined pulse widths as a form of crude spatial localization to achieve a 90 degree pulse at the chosen region. Sample material located more than one coil radius away from the surface coil generally does not contribute to the spectrum. The signal-to-noise achieved with surface coils is very good due to their excellent filling factor, and can be

influenced by the geometry of the coil as well as the material used for the coil wire. A silver plated copper wire yields surface coils of higher Q and signal-to-noise than pure copper coils. In view of the science of surface coils themselves, it seems imperative at this point to use surface coils which have been designed strictly to the requirements of the sample and experiment. Coil geometries as well as the use of two or more coils in various configurations should be explored as possible means to achieve the type of B_1 field desired. The B_1 field shape should determine the coil design. However, relative simplicity in coil design appears to be the current and appropriate goal with more emphasis placed on using suitable pulse sequences for obtaining localized signals from the sensitive volume.

The fact that metabolic deviations can be detected by NMR is encouraging enough to pursue its potential applications. It has been shown that ^{31}P NMR is sensitive to changes in oxygen uptake of muscles and drastic metabolic deviations of the brain. However, the effects of kainic acid were not observed with this technique. Lack of any spectral evidence for the altered tissue implies that the insult was not severe enough to be manifest as a positive indicator; or that the insult does not affect the metabolic chemistry of the brain. The latter hypothesis may be explored further by ^{1}H or other NMR sensitive nuclei before a hypothesis on the action of

KA can be advanced.

Most of the NMR results published to date on aberrant metabolic states show the same spectral indicator. That is, the increase of the inorganic phosphate peak with a concommitant decrease of the phosphocreatine peak. Without foreknowledge of the particular disease or sample preparation it would be impossible to use these ^{31}P spectra diagnostically; rather only as a confirmation that some abnormal state existed. Until ^{31}P NMR can be developed as a reliable quantitative tool, where concentrations of energy metabolites can be accurately calculated, many unrelated diseased tissues will appear undifferentiated by a ^{31}P NMR spectrum. The use of other nuclei as probes in this case would help to clarify the situation.

Further studies of *in-vivo* systems with ^{31}P NMR spectroscopy using surface coils will continue to map the ^{31}P profile of various body parts and organs. The next step may be to perform slightly more invasive experiments, such as injecting a metabolite into the body of a diseased animal to show how the disease affects metabolism in more detail. This could be a temporary tangent which is likely to follow if finer resolution of the ^{31}P spectrum is not attained, especially in the region downfield from the PCr peaks. More data analysis of the spectrum itself may yield illuminating indicators

about the mechanics of metabolism. Factors such as peak height ratios and relative peak intensities may be examined in more detail to reveal useful information previously overlooked or unavailable. Before ^{31}P NMR can be used as a clinical diagnostic tool, standards of spectra must be tabulated as statistical averages of many samples. The natural biological variation within a species should be recorded as a "normal" spectrum before an abnormal metabolic state can be identified. In the long term, *in-vivo* ^{31}P surface coil spectroscopy will undoubtedly yield much information about metabolic status and will be a very desirable non-invasive clinical diagnostic tool.

REFERENCES

1. P.C. Lauterbur, *Nature 242*, 190,1973.

2. P.C. Lauterbur, D.M. Kramer, W.V. House, Jr., and C-N. Chen, *J. Am. Chem. Soc. 97*, 6866, 1975.

3. P. Bendell, C.M. Lai and P.C. Lauterbur, *J. Mag. Reson. 38*, 343, 1980.

4. J.J.H. Ackerman, T.H. Grove, G.G. Wong, D.G. Gadian and G.K. Radda, *Nature 283*,167-170, 1980.

5. P. Plateau and M. Gueron, *J. Am. Chem. Soc. 104*, 7310, 1982.

6. P.J. Hore, *J. Mag. Reson.*, *54*, 539, 1982.

7. S.M. Cohen *in* Society of Magnetic Resonance in Medicine, Third Annual Meeting Aug. 13-17, 1984, pp. 166.

8. K.J. Neurohr, *J. Mag. Reson. 59*, 511, 1984.

9. N.V. Reo, B.A. Seigfried, C.S. Ewy, and J.J.H. Ackerman *in* Society of Magnetic Resonance in Medicine, Third Annual Meeting Aug. 13-17, 1984, pp 615.

10. D.L. Rothman, K.L. Behar, H.P. Hetherington, J.A. den Hollander, M.R. Bendall, and R.G. Shulman *in* Society of Magnetic Resonance in Medicine, Third Annual Meeting Aug. 13-17, 1984, pp. 639.

11. W.R. Adam, A.P. Koretsky, and M.W. Weiner *in* Society of Magnetic Resonance in Medicine, Third Annual Meeting Aug. 13-17, 1984, pp. .

12. D.F. Dedrick, C.S. Springer, M.M. Pike, T.W. Smith, and P.D. Allen *in* Society of Magnetic Resonance in Medicine, Third Annual Meeting Aug. 13-17, 1984, pp. 183.

13. J.A. den Hollander, K.L. Behar, R.G. Shulman, *J. Mag. Reson. 57*, 311, 1984.

14. R.E. Gordon, P.E. Hanley, D. Shaw, D.G. Gadian, G.K. Radda, P. Styles, P.J. Bore, and L. Chan, *Nature 287*, 736, 1980.

15. W.S. Hinshaw, *Phys. Lett. 448*, 87, 1974.

16. R.E. Gordon, P.E. Hanley and D. Shaw, *Prog. in NMR*

Spec. 15, 1, 1982.

17. D.I. Hoult, *J. Mag. Reson. 33*, 183, 1979.

18. M.R. Bendall, *Chem. Phys. Letts. 99*, 310, 1983.

19. M.R. Bendall and R.E. Gordon, *J. Mag. Reson. 53*, 365, 1983.

20. M.R. Bendall and W.P. Aue, *J. Mag. Reson. 54*, 149, 1983.

21. M.R. Bendall, *J. Mag. Reson. 59*, 406, 1984.

22. P.A. Bottomley, T.B. Foster and R.D. Darrow, *J. Mag. Reson. 59*, 338, 1984.

23. J.L. Evelhoch, M.G. Crowley and J.J.H. Ackerman, *J. Mag. Reson. 56*, 110, 1984.

24. A. Haase, W. Hanicke, J. Frahm, *J. Mag. Reson. 56*, 401, 1984.

25. W.R. Smythe, "Static and Dynamic Electricity", 3rd ed. McGraw-Hill, New York, 1968. pp. 291.

26. D.I. Hoult and R.E. Richards, *J. Mag. Reson. 24*, 71, 1976.

27. D.I. Hoult, *J. Mag. Reson. 35*, 69, 1979.

28. D. Shaw, "Fourier Transform N.M.R. Spectroscopy" Elsevier, Amsterdam, 1976.

29. B. Grob, "Basic Electronics" Third Ed., McGraw-Hill, N.Y., 1971. pp. 564.

30. T.M. Grist and J.S. Hyde, *J. Mag. Reson. 61*, 571, 1985.

31. M. Garwood, T. Schleich, G.B. Matson, and G. Acosta, *J. Mag. Reson. 60* , 268-279, 1984.

32. T. Yoshida, E. Fukushima, and J. Brainard *in* 26th Experimental NMR Conference April 21-25, 1985, (A79).

33. A.J. Shaka, J. Keeler, M.B. Smith and R. Freeman, *J. Mag. Reson. 61*, 175, 1985.

34. Ross et al. *New Eng. J. Med. 304*, 1338, 1981.

35. R. Moon and J. Richards, *J. Biol. Chem. 248*, 7276, 1973.

36. D.G. Gadian, "Nuclear Magnetic Resonance and its Applications to Living Systems", Clarendon Press, Oxford, 1982.

37. A.H. Lehninger, "Biochemistry", Worth, New York, 1970.

38. R. Nunnally and P.A.Bottomely, *Science 211*, 177, 1981.

39. G.K. Radda, P.J. Bore, B. Rajagopalan, *Brit. Med. Bull. 40*, 155, 1983.

40. B. Chance, J.S. Leigh Jr., S. Nioka, V.H. Subramanian, J. Maris, G. Whitman, R. Kelley, B.J. Clark, H. Bode, N.R.M. Buist, N. Kennaway, *Fed. Proc. 43*, 316, 1984.

41. S. Naruse, S. Takada, I. Koizuka, H. Watari, *Jap. J. Physiol. 33*, 19, 1983.

42. R.K. Deuel, G.M. Yue, W.R. Sherman, D.J. Schickner, and J.J.H. Ackerman, *Science 228*, 1329, 1985.

43. I.D. Campbell and C.M. Dobson *in* "Methods of Biochemical Analysis" pp. 1.

44. J.J.H. Ackerman, J.L. Evelhoch, B.A. Berkowitz, G.M. Kichura, R.K. Deuel, and K.S. Lown, *J. Mag. Reson. 56*, 318, 1984.

45. "Kainic Acid as a Tool in Neurobiology" (E.G. McGeer, J.W. Wolney, and P.L. McGeer, Eds.), Raven Press, New York, 1978.

46. J.J.H. Ackerman, D.G. Gadian, G.K. Radda, and G.G. Wong, *J. Mag. Reson. 42*, 498, 1981.

47. J.J.H. Ackerman, B.A. Berkowitz, and R.K. Deuel, *Biochem. and Biophys. Res. Comm. 119*, 913, 1984.

48. K.M. Brindle, J. Boyd, I.D. Campbell, R. Porteous, and N. Soffe, *Biochem. and Biophys. Res. Comm. 109*, 864, 1982.

49. N.V. Reo, C.S. Ewy, B.A. Seigfried, J.J.H. Ackerman, *J. Mag. Reson. 58*,76, 1984.

50. W. Westler and J.L. Markley, *J. Mag. Reson. 57*, 519, 1984.

51. R. Gonzalo-Mendez, L. Litt, A.P. Koretsky, J. von Colditz, M.W. Weiner, and T.L. James, *J. Mag. Reson. 57*, 526, 1984.

52. S. Naruse, Y. Horikawa, C. Tanaka, K. Hirakawa, H. Nishikawa, K. Yoshizaki, *J. of Neurosurgery 56*, 747, 1982.

53. E.B. Cady, M.J. Dawson, P.L. Hope, P.S. Tofts, A.M. Costello, D.T. Delpy, E.O.R. Reynolds, and D.R. Wilkie *Lancet* 14 May 1983 pp. 1059.

54. J.W. Pritchard, J.R. Alger, K.L. Behar, O.A.C. Petroff, and R.G. Shulman, *Proc. Natl. Acad. Sci. 80*, 2748, 1983.

55. K.L. Behar, J.A. den Hollander, and R.G. Shulman, *Proc. Natl. Acad. Sci. 80* , 4945, 1983.

56. R. Tycko and A. Pines, *J. Mag. Reson. 60*, 156, 1984.

57. J.K. Gard and J.J.H. Ackerman, *J. Mag. Reson. 51*, 124, 1983.

58. K.R. Thulborn and J.J.H. Ackerman, *55*, 357,1983.

59. J.L. Evelhoch and J.J.H. Ackerman, *J. Mag. Reson. 53*, 52, 1983.

60. D.I. Hoult and P.C.Lauterbur, *J. Mag. Reson. 34*, 425, 1979.

61. D.G. Gadian and F.N.H. Robinson, *J. Mag. Reson. 34*, 449, 1979.

62. S.J. Cox and P. Styles, *J. Mag. Reson. 40*, 209, 1980.

63. A. Haase, C. Malloy and G.K. Radda, *J. Mag. Reson. 55*, 164, 1983.

64. D.L. Rothman, F. Arias-Mendoza, G.I. Shulman, and R.G. Shulman, *J. Mag. Reson. 60*, 430, 1984.

65. M.R. Bendall, J.M. McKendry, I.D. Cresshull, R.J. Odridge, *J. Mag. Reson. 60*, 473, 1984.

66. A. Haase, *J. Mag. Reson. 60*, 130, 1984.

67. W.J. Thoma, L.M. Henderson, and K. Ugurbil, *J. Mag. Reson. 61*, 141, 1985.

68. J.C. Haselgrove, V.H. Subramanian, J.S. Leigh Jr., L. Gyulai, B. Chance, *Science 220*, 1170, 1983.

69. C.T. Turner and P.B. Garlick, *J. Mag. Reson. 57*, 221, 1984.

70. G.K. Radda, D.G. Gadian and P. Styles *in* "NMR Imaging: Proceedings of an International Symposium on NMR Imaging", Bowman Gray School of Medicine, 1981, pp. 159.

71. R.L. Nunnally *in* "NMR Imaging: Proceedings of an International Symposium on NMR Imaging" Bowman Gray School of Medicine, 1981. pp. 181.

72. D.L. Arnold, P.M. Matthews, G.K. Radda, *J. Mag. Reson. in Med. 1*, 307, 1984.

73. G.K. Radda, P.J. Bore, D.G. Gadian, B.D. Ross, P. Styles, D.J. Taylor and J. Morgan-Hughes, *Nature 295*, 608, 1982.

74. K.N. Scott, H.R. Brooker, J.R. Fitzsimmons, H.F. Bennett and R.C. Mick, *J. Mag. Reson. 50*, 339, 1982.

75. D.G. Gadian, G.K. Radda, R.E. Richards and P.J. Seeley *in* "Biological Applications of Magnetic Resonance", Academic Press, 1976, pp. 463.

76. S. Naruse, Y. Horikawa, C. Tanaka, K. Hirakawa, H. Nishikawa and H. Watari, *Brain Research, 296*, 370, 1984.

77. D.T. Delpy, R.E. Gordon, P.L. Hope,*Pediatrics 70*,310, 1982.

78. R.K. Deuel, G.M. Yue, W.R. Sherman, D.J. Schickner, and J.J.H. Ackerman, *Science 228*, 1329, 1985.

79. M.A. Foster, "Magnetic Resonance in Medicine and Biology", Pergamon Press, London, 1984.

80. R.S. Balaban, D.G. Gadian, and G.K. Radda, *Kidney Int. 20*, 575, 1981.

81. P. Styles, M.B. Smith, R.W. Briggs, and G.K. Radda, *J. Mag. Reson. 62*, 397, 1985.

APPENDIX

The derivation of the vector potential and field of a circular loop of wire was outlined by Smythe[25] and used by others[4 3 1] to calculate the B_1 field of surface coils.

For a point, P, located in the yz plane above the coil in the figure below, at a radial distance, ρ, from the coil center, Smythe finds the axial, B_a, and radial, B_ρ, fields to be:

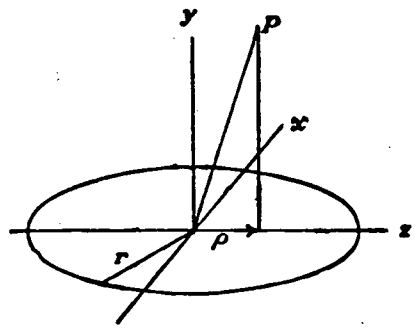

$$B_a = \frac{\mu I}{2\pi} \frac{y}{\rho[(r+\rho)^2 + y^2]^{1/2}} \left[-K + \frac{r^2 + \rho^2 + y^2}{(r-\rho)^2 + y^2} E \right] \quad \text{(i)}$$

$$B_\rho = \frac{\mu I}{2\pi} \frac{1}{[(r+\rho)^2 + y^2]^{1/2}} \left[K + \frac{r^2 - \rho^2 - y^2}{(r-\rho)^2 + y^2} E \right] \quad \text{(ii)}$$

where μ is the permeability of the medium surrounding the coil, I is the current flowing through the coil, r, the coil radius, and K and I, the complete elliptical integrals of the first and second kind, respectively.

In the calculation of B_1 contours for this thesis, the following assumptions and substitutions were made:

(1) unit current was assumed to be flowing through the coil wire, hence I=1;
(2) coil radius, r=1;
(3) the distance, ρ, which was a variable in this case, was set to
(4) the distance from the coil center to the point, P, was then

To simplify the calculation in the FORTRAN programs used, the arbitrary variables, A, B, C, and D were set to portions of the equation:

$$A = \frac{(1 + x^2 + y^2 + z^2)}{[1 - (x^2+z^2)^{1/2}]^2 + y^2}$$

$$B = \frac{1}{\{[1 + (x^2+z^2)^{1/2}]^2 + y^2\}^{1/2}}$$

$$C = \frac{y}{(x^2+y^2)^{1/2}}$$

$$D = \frac{(1 - x^2 - y^2 - z^2)}{[1 - (x^2+z^2)^{1/2}]^2 + y^2}$$

The following programs list equations (i) and (ii) as:

$$B_a = (E \times D + K) \times B \qquad (i)*$$

$$B_r = (E \times A - K) \times B \times C \qquad (ii)*$$

```
      C THIS PROGRAM CALCULATES THE COMPONENTS OF A MAGNETIC FIELD
      C INDUCED BY A UNIT CURRENT RUNNING IN A CIRCULAR LOOP
            DIMENSION XP(201),YP(101),ZP(201,101)
            PI=4.*ATAN(1.0)
      C
      C
      C
      C
      CC
      C
      C
            Z=0.5
              DO 400 J=1,201
              X=(FLOAT(J)-101.)/50.
      C
                DO 300 K=1,101
                Y=(FLOAT(K)-1.)/50.0
      C
                IR=1
      C
                XZ=SQRT(X**2+Z**2)
      C
      C
      C check for points on the ring
      C
      C
            IF((ABS(XZ-1.0).LE.10E-6).AND.(K.EQ.1)) GO TO 300
            A=(1.+X**2+Y**2+Z**2)/((1.-XZ)**2+Y**2)
      C
            B=1./SQRT((1.+XZ)**2+Y**2)
      C
            D=(1.-X**2-Y**2-Z**2)/((1.-XZ)**2+Y**2)
      C
            IF(K.NE.1) GO TO 140
            C=0.0
      C
            GO TO 180
      C
      C check for points on the axis
      C
       140  IF((XZ-0.).GT.10E-6) GO TO 170
            IR=0
            GO TO 180
       170  C=Y/XZ
       180  XISQ=4.*XZ/((1.+XZ)**2+Y**2)
            XI=SQRT(XISQ)
            EF1=ELIK1(XI,IND1)
            ES1=ELIE1(XI,IND2)
            IF(IR.EQ.1) GO TO 190
            BRAD=0.0
            GO TO 195
       190  BRAD=(ES1*A-EF1)*B*C
       195  BAX=(ES1*D+EF1)*B
      54.5  THETA=ATAN(-X/Z)
      55    C     IF(J.NE.21) THETA=PI/2.
      56    C     IF(J.EQ.21) THETA=0.0
      57          BX=BRAD*SIN(THETA)
      58          BY=BAX
      59          B1=SQRT(BX**2+BY**2)
      60          ZP(J,K)=B1
      61          RA=BX/BY
      62          ALPHA=ATAN(RA)*180.0/PI
      63    C
      64    C
      65    C
      66    C
      67    C
      68          GO TO 300
      69    C
      70    C
       300  CONTINUE
       400  CONTINUE
              DO 800 M=1,101
       800    YP(M)=(FLOAT(M)-1.)/50.0
              DO 850 L=1,201
       850    XP(L)=(FLOAT(L)-101.)/50.
      C
              CALL AXIS(-2.0,0.0,1HX,-1,4.0,0.0,-2.0,1.0)
              CALL AXIS(0.0,0.0,1HY,1,2.0,90.0,0.0,1.0)
              DO 950 I=1,500
              CN=FLOAT(I)
              CALL CNTOUR(XP,201,YP,101,ZP,201,CN,0.0,CN)
       950    CONTINUE
              CALL PLOTND
      C
            STOP
            END
```

```
C THIS PROGRAM CALCULATES THE COMPONENTS OF A MAGNETIC FIELD
C INDUCED BY A UNIT CURRENT RUNNING IN A DOUBLE LOOP.
      DIMENSION XP(201),YP(101),ZP(201,101)
      PI=4.*ATAN(1.0)
      R=0.6
C     WRITE(6,100)
C100  FORMAT(/3X,'X1',6X,'Y1',6X,'Z1',6X,'X2',6X,'Y2',6X,'Z2',6X,
C    * 'BX1',5X,'BY1',5X,'B11',5X,
C    * 'B1',6X,'ALPHA',3X,'BETA',4X,'GAMMA'/)
C     DO 600 I=1,3
      Z1=0.5
      Z2=Z1/R
        DO 500 J=1,201
        X1=(FLOAT(J)-101.)/50.
        X2=X1/R
          DO 400 K=1,101
          Y1=(FLOAT(K)-1.0)/50.
          Y2=Y1/R
          IR1=1
          IR2=1
          XZ1=SQRT(X1**2+Z1**2)
          XZ2=SQRT(X2**2+Z2**2)
C
C check for points on the ring
C
      IF((ABS(XZ1-0.6).LE.10E-3).AND.(K.EQ.1)) GO TO 400
      IF((ABS(XZ1-1.0).LE.10E-3).AND.(K.EQ.1)) GO TO 400
      IF((ABS(XZ2-1.0).LE.10E-3).AND.(K.EQ.1)) GO TO 400
      IF((ABS(XZ2-1.6).LE.10E-3).AND.(K.EQ.1)) GO TO 400
      A1=(1.+X1**2+Y1**2+Z1**2)/((1.-XZ1)**2+Y1**2)
      A2=(1.+X2**2+Y2**2+Z2**2)/((1.-XZ2)**2+Y2**2)
      B1=1./SQRT((1.+XZ1)**2+Y1**2)
      B2=1./SQRT((1.+XZ2)**2+Y2**2)
      D1=(1.-X1**2-Y1**2-Z1**2)/((1.-XZ1)**2+Y1**2)
      D2=(1.-X2**2-Y2**2-Z2**2)/((1.-XZ2)**2+Y2**2)
      IF(K.NE.1) GO TO 140
      C1=0.0
      C2=0.0
      GO TO 180
C
C check for points on the axis
C
 140  IF((XZ1-0.0).GT.10E-6) GO TO 170
      IR1=0
      GO TO 180
 170  C1=Y1/XZ1
 180  XISQ1=4.*XZ1/((1.+XZ1)**2+Y1**2)
      XI1=SQRT(XISQ1)
      EF1=ELIK1(XI1,IND1)
      ES1=ELIE1(XI1,IND2)
      IF(IR1.EQ.1) GO TO 190
      BRAD1=0.0
      GO TO 195
 190  BRAD1=(ES1*A1-EF1)*B1*C1
 195  BAX1=(ES1*D1+EF1)*B1
      THETA=ATAN(-X1/Z1)
C     IF(J.NE.1) THETA=PI/2.
C     IF(J.EQ.1) THETA=0.0
      BX1=BRAD1*SIN(THETA)
      BY1=BAX1
      B11=SQRT(BX1**2+BY1**2)
      RA1=BX1/BY1
      ALPHA=ATAN(RA1)*180.0/PI
C
      IF((XZ2-0.0).GT.10E-6) GO TO 270
      IR2=0
      GO TO 280
 270  C2=Y2/XZ2
 280  XISQ2=4.*XZ2/((1.+XZ2)**2+Y2**2)
      XI2=SQRT(XISQ2)
      EF2=ELIK1(XI2,IND1)
      ES2=ELIE1(XI2,IND2)
      IF(IR2.EQ.1) GO TO 290
      BRAD2=0.0
      GO TO 295
 290  BRAD2=(ES2*A2-EF2)*B2*C2
 295  BAX2=(ES2*D2+EF2)*B2
      PHI=ATAN(-X2/Z2)
C     IF(J.NE.1) PHI=PI/2.
C     IF(J.EQ.1) PHI=0.0
      BX2=BRAD2*SIN(PHI)
      BY2=BAX2
      B12=SQRT(BX2**2+BY2**2)
      RA2=BX2/BY2
      BETA=ATAN(RA2)*180.0/PI
C
C sum of small and large fields
C
      BX=BX1+BX2
      BY=BY1+BY2
      B1=SQRT(BX**2+BY**2)
      ZP(J,K)=B1
      RATIO=BX/BY
      GAMMA=ATAN(RATIO)*180.0/PI
C     WRITE(6,300) X1,Y1,Z1,X2,Y2,Z2,BX1,BY1,B11,B1,
C    *ALPHA,BETA,GAMMA
C300  FORMAT(10F8.4,3F8.2)
      GO TO 400
C490  WRITE(6,495) X1,Y1,Z1
C495  FORMAT(/'(X1,Y1,Z1)= ',3F5.2,' , point is on the larger
C    *ring'/)
C     GO TO 400
C590  WRITE(6,595) X2,Y2,Z2
C595  FORMAT(/'(X2,Y2,Z2)= ',3F5.2,' , point is on the smaller
C    *ring'/)
 400  CONTINUE
 500  CONTINUE
      DO 800 M=1,101
 800  YP(M)=(FLOAT(M)-1.)/50.0
      DO 850 L=1,201
 850  XP(L)=(FLOAT(L)-101.)/50.
      CALL AXIS(-2.0,0.0,1HX,-1,4.0,0.0,-2.0,1.0)
      CALL AXIS(0.0,0.0,1HY,1,2.0,90.0,0.0,1.0)
      DO 950 I=1,500
      CN=FLOAT(I)
      CALL CNTOUR(XP,201,YP,101,ZP,201,CN,0.0,CN)
 950  CONTINUE
      CALL PLOTND
      STOP
      END
```

```
      C THIS PROGRAM CALCULATES THE COMPONENTS OF A MAGNETIC FIELD
      C INDUCED BY A UNIT CURRENT RUNNING IN A 0.9 COIL DIAM=2.0
            DIMENSION XP(201),YP(101),ZP(201,101)
            PI=4.*ATAN(1.0)
            R=0.9
      C     WRITE(6,100)
      C100  FORMAT(/3X,'X1',6X,'Y1',6X,'Z1',6X,'X2',6X,'Y2',6X,'Z2',6X,
      C     * 'BX1',5X,'BY1',5X,'B11',5X,
      C     * 'B1',6X,'ALPHA',3X,'BETA',4X,'GAMMA',3X,'B1REL'/)
      C
            Z1=0.0
            Z2=0.0
              DO 500 J=1,201
              X1=(FLOAT(J)-101.)/50.
              X2=X1/R
                DO 400 K=1,101
                Y1=(FLOAT(K)-1.0)/50.
                Y2=Y1/R
                IR1=1
                IR2=1
                XZ1=SQRT(X1**2+Z1**2)
                XZ2=SQRT(X2**2+Z2**2)
            Q=SQRT(X1**2+Y1**2+Z1**2)
            Q1=SQRT(X1**2+0.0625)
      C
      C check for points on the ring
      C
            IF((ABS(XZ2-1.0).LE.10E-3).AND.(K.EQ.1)) GO TO 400
            IF(ABS(Q1-1.0307764).LE.10E-3) GO TO 400
            A1=(1.+X1**2+Y1**2+Z1**2)/((1.-XZ1)**2+Y1**2)
            A2=(1.+X2**2+Y2**2+Z2**2)/((1.-XZ2)**2+Y2**2)
            B1=1./SQRT((1.+XZ1)**2+Y1**2)
            B2=1./SQRT((1.+XZ2)**2+Y2**2)
            D1=(1.-X1**2-Y1**2-Z1**2)/((1.-XZ1)**2+Y1**2)
            D2=(1.-X2**2-Y2**2-Z2**2)/((1.-XZ2)**2+Y2**2)
            IF(K.NE.1) GO TO 140
            C1=0.0
            C2=0.0
            GO TO 180
      C
      C check for points on the axis
      C
       140  IF((XZ1-0.0).GT.10E-6) GO TO 170
            IR1=0
            GO TO 180
       170  C1=Y1/XZ1
       180  XISQ1=4.*XZ1/((1.+XZ1)**2+Y1**2)
            XI1=SQRT(XISQ1)
            EF1=ELIK1(XI1,IND1)
            ES1=ELIE1(XI1,IND2)
            IF(IR1.EQ.1) GO TO 190
            BRAD1=0.0
            GO TO 195
        190 BRAD1=(ES1*A1-EF1)*B1*C1
        195 BAX1=(ES1*D1+EF1)*B1
      C
            IF(J.NE.1) THETA=PI/2.
            IF(J.EQ.1) THETA=0.0
            BX1=BRAD1*SIN(THETA)
            BY1=BAX1
            B11=SQRT(BX1**2+BY1**2)
            RA1=BX1/BY1
            ALPHA=ATAN(RA1)*180.0/PI
      C
            IF((XZ2-0.0).GT.10E-6) GO TO 270
            IR2=0
            GO TO 280
       270  C2=Y2/XZ2
       280  XISQ2=4.*XZ2/((1.+XZ2)**2+Y2**2)
            XI2=SQRT(XISQ2)
            EF2=ELIK1(XI2,IND1)
            ES2=ELIE1(XI2,IND2)
            IF(IR2.EQ.1) GO TO 290
            BRAD2=0.0
            GO TO 295
       290  BRAD2=(ES2*A2-EF2)*B2*C2
       295  BAX2=(ES2*D2+EF2)*B2
      C
            IF(J.NE.1) PHI=PI/2.
            IF(J.EQ.1) PHI=0.0
            BX2=BRAD2*SIN(PHI)
            BY2=BAX2
            B12=SQRT(BX2**2+BY2**2)
            RA2=BX2/BY2
            BETA=ATAN(RA2)*180.0/PI
      C
      C sum of small and large fields
      C
            BX=BX1+BX2
            BY=BY1+BY2
            B1=SQRT(BX**2+BY**2)
            ZP(J,K)=B1
            RATIO=BX/BY
            GAMMA=ATAN(RATIO)*180.0/PI
      C     WRITE(6,300) X1,Y1,Z1,X2,Y2,Z2,BX1,BY1,B11,B1,
      C     *ALPHA,BETA,GAMMA
      C300  FORMAT(10F8.4,3F8.2
      C     GO TO 400
      C490  WRITE(6,495) X1,Y1,Z1
      C495  FORMAT(/'(X1,Y1,Z1)= ',3F5.2,' , point is on the larger
      C     *ring'/)
      C     GO TO 400
      C590  WRITE(6,595) X2,Y2,Z2
      C595  FORMAT(/'(X2,Y2,Z2)= ',3F5.2,' , point is on the smaller
      C     *ring'/)
       400  CONTINUE
       500  CONTINUE
            DO 800 M=1,101
       800  YP(M)=(FLOAT(M)-1./50.)
            DO 850 L=1,201
       850  XP(L)=(FLOAT(L)-101./50.)
            CALL AXIS(-2.0,0.0,1HX,1,100.0,0.0,-2.0,1.0)
            CALL AXIS(-2.0,0.0,1HY,-1,36.0,90.0,0.0,1.0)
            DO 900 I=1,500
            CN=FLOAT(I)
            CALL CNTOUR(XP,201,YP,101,ZP,201,CN,1.0,CN)
       900  CONTINUE
            CALL PLOTND
      C
            STOP
            END
```

```
      C THIS PROGRAM CALCULATES THE COMPONENTS OF A MAGNETIC FIELD
      C INDUCED BY A UNIT CURRENT RUNNING IN A 0.9 COIL DIAM=2.0
            DIMENSION XP(161),YP(85),ZP(161,85)
            PI=4.*ATAN(1.0)
            R=1.0
      C     WRITE(6,100)
      C100  FORMAT(/3X,'X1',6X,'Y1',6X,'Z1',6X,'X2',6X,'Y2',6X,'Z2',6X,
      C    * 'BX1',5X,'BY1',5X,'B11',5X,
      C    * 'B1',6X,'ALPHA',3X,'BETA',4X,'GAMMA',3X,'B1REL'/)
      C
            Z1=0.5
            Z2=Z1/R
              DO 500 J=1,161
              X1=((FLOAT(J)*25.)-2025.)/1000.
              X2=X1/R
                DO 400 K=1,85
                Y1=((FLOAT(K)*25.)-125.)/1000.
                Y2=(((FLOAT(K)*25.)-25.)/1000.)/R
                IR1=1
                IR2=1
                XZ1=SQRT(X1**2+Z1**2)
                XZ2=SQRT(X2**2+Z2**2)
            Q=SQRT(X1**2+Y1**2+Z1**2)
            Q1=SQRT(X1**2+Y1**2)
      C
      C check for points on the ring
      C
            IF((ABS(XZ2-1.0).LE.10E-6).AND.(K.EQ.1)) GO TO 400
            IF((ABS(Q1-0.871779).LE.10E-6).AND.(K.EQ.1))GO TO 400
            IF((ABS(1.-XZ1).LE.10E-6).AND.(K.EQ.5)) GO TO 400
            IF((ABS(XZ1-0.8660254).LE.10E-6).AND.(K.EQ.5))GO TO 400
            IF((ABS(Q1-0.8660254).LE.10E-6).AND.(K.EQ.5))GO TO 400
            A1=(1.+X1**2+Y1**2+Z1**2)/((1.-XZ1)**2+Y1**2)
            A2=(1.+X2**2+Y2**2+Z2**2)/((1.-XZ2)**2+Y2**2)
            B1=1./SQRT((1.+XZ1)**2+Y1**2)
            B2=1./SQRT((1.+XZ2)**2+Y2**2)
            D1=(1.-X1**2-Y1**2-Z1**2)/((1.-XZ1)**2+Y1**2)
            D2=(1.-X2**2-Y2**2-Z2**2)/((1.-XZ2)**2+Y2**2)
            IF(K.NE.1) GO TO 140
            C1=0.0
            C2=0.0
            GO TO 180
      C
      C check for points on the axis
      C
       140  IF((XZ1-0.0).GT.10E-6) GO TO 170
            IR1=0
            GO TO 180
       170  C1=Y1/XZ1
       180  XISQ1=4.*XZ1/((1.+XZ1)**2+Y1**2)
            XI1=SQRT(XISQ1)
            EF1=ELIK1(XI1,IND1)
            ES1=ELIE1(XI1,IND2)
            IF(IR1.EQ.1) GO TO 190
            BRAD1=0.0
            GO TO 195
       190  BRAD1=(ES1*A1-EF1)*B1*C1
        195 BAX1=(ES1*D1+EF1)*B1
            THETA=ATAN(-X1/Z1)
      C     IF(J.NE.1) THETA=PI/2.
      C     IF(J.EQ.1) THETA=0.0
            BX1=BRAD1*SIN(THETA)
            BY1=BAX1
            B11=SQRT(BX1**2+BY1**2)
            RA1=BX1/BY1
            ALPHA=ATAN(RA1)*180.0/PI
      C
            IF((XZ2-0.0).GT.10E-6) GO TO 270
            IR2=0
            GO TO 280
       270  C2=Y2/XZ2
       280  XISQ2=4.*XZ2/((1.+XZ2)**2+Y2**2)
            XI2=SQRT(XISQ2)
            EF2=ELIK1(XI2,IND1)
            ES2=ELIE1(XI2,IND2)
            IF(IR2.EQ.1) GO TO 290
            BRAD2=0.0
            GO TO 295
        290 BRAD2=(ES2*A2-EF2)*B2*C2
        295 BAX2=(ES2*D2+EF2)*B2
            PHI=ATAN(-X2/Z2)
      C     IF(J.NE.1) PHI=PI/2.
      C     IF(J.EQ.1) PHI=0.0
            BX2=BRAD2*SIN(PHI)
            BY2=BAX2
            B12=SQRT(BX2**2+BY2**2)
            RA2=BX2/BY2
            BETA=ATAN(RA2)*180.0/PI
      C
      C sum of small and large fields
      C
            BX=BX1+BX2
            BY=BY1+BY2
            B1=SQRT(BX**2+BY**2)
            ZP(J,K)=B1
            RATIO=BX/BY
            GAMMA=ATAN(RATIO)*180.0/PI
      C     WRITE(6,300) X1,Y1,Z1,X2,Y2,Z2,BX1,BY1,B11,B1,
      C    *ALPHA,BETA,GAMMA
      C300  FORMAT(10F8.4,3F8.2
      C     GO TO 400
      C490  WRITE(6,495) X1,Y1,Z1
      C495  FORMAT(/'(X1,Y1,Z1)= ',3F5.2,' , point is on the larger
      C    *ring'/)
      C     GO TO 400
      C590  WRITE(6,595) X2,Y2,Z2
      C595  FORMAT(/'(X2,Y2,Z2)= ',3F5.2,' , point is on the smaller
      C    *ring'/)
        400 CONTINUE
        500 CONTINUE
            DO 800 M=1,85
        800 YP(M)=((FLOAT(M)*25.)-125.)/1000.
            DO 850 L=1,161
        850 XP(L)=((FLOAT(L)*25.)-2025.)/1000.
            CALL AXIS(-2.0,-0.10,1HX,-1,4.0,0.0,-2.0,1.0)
            CALL AXIS(0.0,-0.10,1HY,1,2.0,90.0,0.0,1.0)
            DO 900 I=1,500
            CN=FLOAT(I)
            CALL CNTOUR(XP,161,YP,85,ZP,161,CN,0.0,CN)
        900 CONTINUE
            CALL PLOTND
      C
            STOP
            END
```